metals

MDPI

Review

Hydrogen Embrittlement of Galvanized Press-Hardened Steels: A Review

Tomáš Kročil [1,*], Nikola Macháčková [1], Tomáš Prošek [1], Thomas Steck [2] and Reza Sharif [2]

[1] The Department of Metals and Corrosion Engineering, Faculty of Chemical Technology, University of Chemistry and Technology Prague, Technicka 5, 160 00 Prague, Czech Republic; machacki@vscht.cz (N.M.); tomas.prosek@vscht.cz (T.P.)

[2] voestalpine Stahl GmbH, voestalpine Strasse 3, 4020 Linz, Austria; thomas.steck@voestalpine.com (T.S.); reza.sharif@voestalpine.com (R.S.)

* Correspondence: tomas.krocil@vscht.cz

Abstract: Press-hardened steels (PHS), as an alternative to traditional steels and aluminum alloys, combine great mechanical performance with low manufacturing costs. PHS are martensitic steels with ultimate tensile strength (UTS) up to 2000 MPa. These steels are commonly coated with zinc-based coatings (PHS GI) consisting of multiple Zn–Fe phases to enhance corrosion resistance. However, similar to all high-strength steels, PHS are known for their elevated susceptibility to hydrogen embrittlement (HE). Absorption of atomic hydrogen into the steel lattice can lead to a transition from a ductile to a brittle fracture mechanism and decrease the stress necessary for fracture initiation. This review examines the microstructure of PHS GI with a focus on how the manufacturing process influences key parameters of the coating. The material's susceptibility to HE is discussed in the following sections, along with the potential for hydrogen introduction through corrosion in atmospheric environments. The relationship between the content of hydrogen and its effects on fracture behavior is discussed, along with the corrosion behavior of PHS GI. The potential areas for future research and development of PHS GI with increased HE resistance are proposed.

Keywords: press hardened steel; martensitic steels; hydrogen embrittlement; atmospheric corrosion

Citation: Kročil, T.; Macháčková, N.; Prošek, T.; Steck, T.; Sharif, R. Hydrogen Embrittlement of Galvanized Press-Hardened Steels: A Review. *Metals* **2024**, *14*, 1285. https://doi.org/10.3390/met14111285

Academic Editors: Fei Yin, Jian Wang and Lin Hua

Received: 30 September 2024
Revised: 4 November 2024
Accepted: 7 November 2024
Published: 12 November 2024

1. Introduction

Advanced high-strength steels (AHSS) have become an essential material in the automotive industry, where they are used mainly for producing passive safety components such as bumpers, A-/B-pillars, etc. [1–3]. Concerning electric cars, AHSS are also used to manufacture battery boxes and their covers to prevent safety and environmental hazards [4]. The excellent mechanical properties of AHSS allow manufacturers to use thinner steel sheets without compromising on safety features, which leads to lighter car body construction and material savings [5]. In the overall weight of a vehicle, steel components take up to 58 wt.%, with about equal mass distribution between the car body and chassis with suspension (excluding the drivetrain) [6]. Fiat Chrysler reported that the share of AHSS in produced cars reached 61% in 2016 [7]. The weight savings by using modern materials such as AHSS and aluminum alloys have a large impact on the reduction in fuel consumption and CO_2 emissions. A 10% weight reduction results in a 5.5% increase in the fuel efficiency [8]. For electric vehicles with batteries weighing 100–200 kg, weight reduction would benefit extended range [9–12]. A minor disadvantage of using AHSS materials can be seen in the process of vehicle manufacturing and repairability because working with these components demands expensive tools and precise control over the welding process [13–16].

Press-hardened steel (PHS) is a type of boron alloyed manganese AHSS that combines a high ultimate tensile strength (UTS) of 1500–2000 MPa with good formability [17]. The high mechanical performance of PHS comes from the manufacturing process, which consists of full austenitization with the subsequent combination of quenching and pressing into

the desired shape. This method called hot stamping gives the steel a fully martensitic microstructure, which provides high strength [18,19]. Steel sheets can be pre-shaped, but the final form of a car part is obtained when the material is pressed by dies. Before the austenitization, steel sheets have a ferritic–pearlitic microstructure, and the ductility of these steels can reach 17%. In a quenched martensitic state, the ductility of the PHS is in a range of 6–7% [6,20–22]. Regardless of the austenitization process, the manufacturing of PHS parts is cheaper in comparison to other materials and high-strength steels [23].

In the automotive industry, these steels are typically protected by metallic coatings. The most common coatings are either Zn–Fe or Al–Si. This review mainly focuses on hot stamped steel coated with hot-dip galvanized zinc (PHS GI), which consists of two Zn–Fe intermetallic phases. The ratio of the phases as well as the thickness of the coating depends on the austenitization parameters [24]. The corrosion behavior of PHS GI is affected by specific features of the coating, which differs from conventional, non-heat-treated, hot-dip galvanized zinc coating. In addition, to obtain galvanic coupling between anodic zinc and cathodic steel, galvanic micro-couples can be established between phases of the PHS GI coating [25]. The PHS GI coating outperforms the commonly used single-phase hot-dip galvanized zinc coating in atmospheric corrosion conditions, but martensitic steels, which are the base of PHS, are more sensitive to the presence of hydrogen [26,27]. A cathodic hydrogen evolution reaction (HER) causes the formation of hydrogen on the surface, which may be absorbed and diffused through the steel. Under increased stress, the content of absorbed hydrogen increases the odds of brittle fracture resulting from hydrogen embrittlement (HE) [28]. The high strength of these steels makes them more susceptible to HE. A brittle fracture below the UTS may negatively impact vehicle safety during a collision [29–31].

This review discusses the relationship between the corrosion behavior of galvanized PHS and the potential risk of HE, especially under atmospheric corrosion conditions. Bare PHS is described in terms of composition, microstructure, and structural defects, which may influence HE. The next section focuses on the relationship between the microstructural features and atmospheric corrosion behavior of coated PHS. The following sections of the review focus on correlating theoretical insights with empirical data concerning the influence of PHS parameters on HE and hydrogen absorption in PHS GI when exposed to corrosive environments.

2. Press Hardened Steels

The race for low-cost manufacturing led the steel industry to develop an efficient way of producing and processing high-strength car parts. To produce a painted car body that is ready for the installation of the engine, electronics, and trim (glass, interior, seats, etc.), the PHS sheet undergoes multiple operations listed in Figure 1.

The manufacturing process starts with a coil of steel sheet. The most commonly used steel for PHS manufacturing, 22MnB5, was originally designed and produced in the 1970s as an abrasion-resistant steel for quenching and tempering. Along with the development of new steel grades, the latest improvements in the mechanical properties of PHS are achieved by advanced regimes of heat treatment and alloying of 22MnB5 steel [32–35]. Other PHS grades that are used, such as 34MnB5, 37MnB4, and 30MnB5, can provide even higher strength compared to 22MnB5 [34,36–38]. Useful features such as improved resistance against excessive oxidation of austenitized steel are provided by newly developed grades, such as 30MnBV [39]. The UTS of PHS over 1500 MPa is reached by combining the martensitic structure and multiple hardening effects by substitutional or interstitial elements, precipitates, refined grains, and dislocations. The elemental composition of PHS is close to conventional carbon steels, as seen in Table 1. The exceptional increase in the strength is caused by an increased content of carbon and boron in a range from 10 to 30 wt. ppm [3]. Boron atoms segregate at the grain boundaries of austenite and block the local heterogeneous nucleation of ferrite [4,40–42]. Adding a small amount of niobium also has a positive effect on the mechanical properties of PHS since it causes grain refinement,

increases toughness, reduces high-temperature grain coarsening, and suppresses cracking during impact or bending [32]. Austenitic grain coarsening can also be suppressed by (Nb, Ti, V)(C, N) precipitates [43].

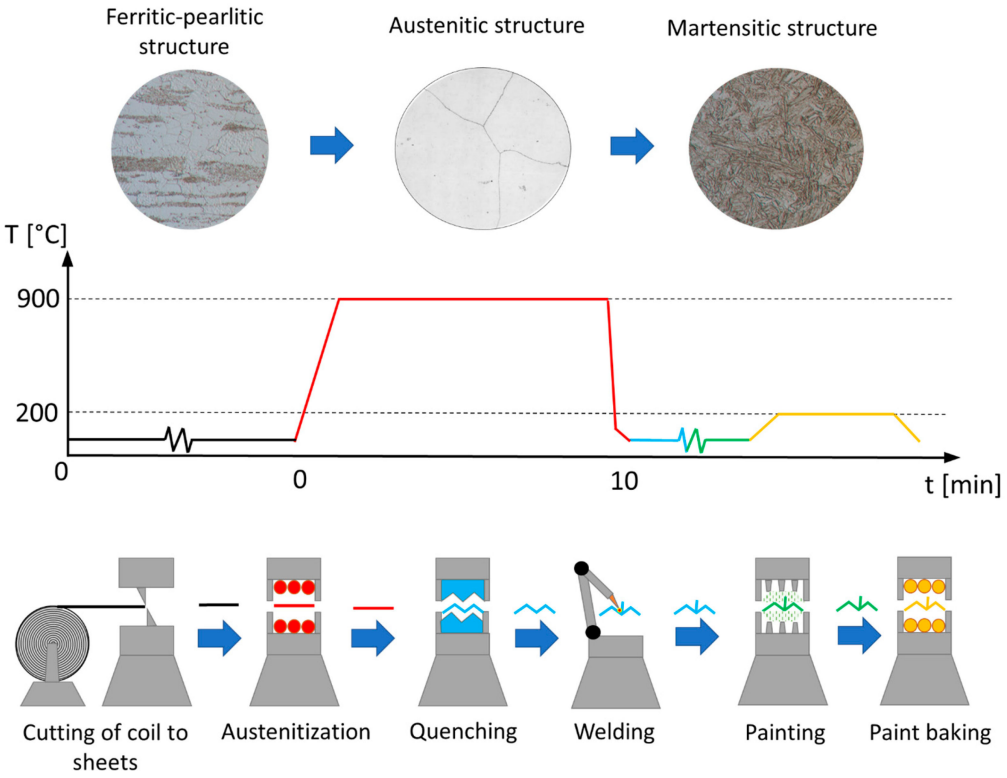

Figure 1. Manufacturing process of PHS parts made of 22MnB5 steel. Temperature line color represents temperature of of sheet during manufacturing process pictured below.

Table 1. Elemental composition of uncoated PHS1500 and PHS2000 [wt.%] Adapted from Ref. [44].

Grade	C	Si Max.	Mn Max.	P Max.	S Max.	Al	Cr Max.	Ti + Nb Max.	B
PHS 1500 (22MnB5)	0.20–0.25	0.5	2.0	0.02	0.005	0.02–0.10	0.5	0.05	0.002–0.005
PHS 2000 (32MnB5)	0.30–0.38	0.5	2.0	0.02	0.005	0.02–0.10	0.5	0.10	0.002–0.005

When the steel coil is unrolled and cut, it undergoes a thermal treatment process called hot stamping, which increases the strength of the steel (see Table 2). The structure and mechanical properties of the quenched steel depend on the parameters of each step. The main factors affecting the strength are the elemental composition, the microstructure of the steel prior to austenitization, and the parameters of austenitization [18]. The hot stamping process is performed with blank sheets of ferritic–pearlitic steel, which are austenitized at temperatures around 900 °C [21]. The dwell time of austenitization is in a range of 3–10 min. Insufficient austenitization caused by low temperature or short dwell time results in a small amount of undissolved pearlite and ferrite, which decreases the fraction of martensite after transformation. Longer annealing time leads to excessive coarsening of austenitic grains [45,46].

Table 2. Mechanical properties of uncoated PHS 1500 and PHS 2000 grade steels before and after the hot stamping process. Adapted from Ref. [44].

Grade	Before Hot Stamping			After Hot Stamping		
	YS [MPa]	UTS [MPa]	Ɛ [%]	YS [MPa]	UTS [MPa]	Ɛ [%]
PHS 1500	320–480	480–600	≥18	950–1250	1350–1600	≥5
PHS 2000	320–500	500–650	≥17	≥1100	≥1800	≥5

UTS: Ultimate tensile strength; YS: Yield strength; Ɛ: Elongation.

A refined martensitic structure can be achieved by a small prior austenite grain (PAG) size of steel. Nucleation of PAGs is supported by the homogenous distribution of pearlite or cementite within the ferritic structure with small, incoherent ferrite grains of steel prior to austenitization [47]. The size of PAGs partially depends on the conditions of austenitization. Correct conditions of austenitization are given by the combination of dwell time and temperature. To eliminate ferritic content under 0.1 vol.%, the temperature of austenitized steel should exceed 850 °C [48]. A temperature of 900 °C seems to ensure a fully martensitic structure with the smallest PAGs, resulting in the best properties of 22MnB5 steel [21]. Helf et al. also pointed out that a temperature interval of 880–910 °C is beneficial for avoiding the formation of undesired lamellar cementite [49]. Higher temperatures cause the growth of austenitic grains and the formation of bulky plane martensite, which results in a lower strength. The common size of PAGs austenitized at temperatures near 900 °C is 5–10 µm and in certain circumstances rises to 60 µm [47,50]. The toughness of steel rapidly increases at a mean PAG size below 40 µm, which is desired [32]. According to the report by Liu et al., an excessive increase in the austenitization temperature from 920 °C to 1020 °C results in an increase in PAG size from 13 to 31 µm, negatively affecting the mechanical performance [51]. Variations in the dwell time of austenitization also affect the final structure of the steel. The best results have been reported for steels with a dwell time close to 5 min. Austenitizing longer than 5 min leads to the growth of PAGs and the loss of toughness and tensile strength [19,49].

Recent studies have focused on changing the volume of austenite, which remains in steel after quenching, known as retained austenite (RA). A small volume of RA from 0.1% up to 4.3% provides better ductility and toughness in combination with the strain-hardening effect. The fraction of RA can be changed by adding Cr and Si, which form finely dispersed carbides. In the austenitized state, the carbides create tiny local chemical gradients of Cr, Si, and C, which can avert martensitic transformation [21,52,53].

After austenitization, the hot sheets are transferred into the pressing machine with cooled copper dies. The process of simultaneous forming and quenching leads to the production of martensitic panels with excellent accuracy and without any springback. To achieve a fully martensitic structure, the cooling rate of a non-deformed sheet has to be 25 °C·s^{-1} or higher [54]. In the automotive industry, where the sheets are also deformed, the critical cooling rate needs to be higher than 30 °C·s^{-1}, but commonly used cooling rates exceed 50 °C·s^{-1}. Furthermore, an increase to 250 °C·s^{-1} does not cause large changes in the strength, ductility, and hardness, which is commonly close to 480 Vickers. A further increase in cooling rate results in a slight improvement in hardness but also an undesired decrease in ductility. The mechanical deformation of steel in an austenitic state contributes to higher hardness and tensile strength [10,26,50,55].

Austenitization and quenching are followed by welding the steel components made of different steel grades to form a car body. Precise control over the welding process is necessary in order to ensure the rigidity of the car body and to avoid excessive hydrogen uptake [5,56–58]. After the welding, the car body is degreased and painted. The paint is later cured in a furnace at 120–200 °C for 10–30 min. Paint baking also improves the mechanical properties of steel by relaxing the residual stress created by the martensitic

transformation and decreasing the amount of hydrogen absorbed into the steel during manufacturing [59–63].

3. Coated PHS

3.1. PHS GI Coating

The corrosion resistance of uncoated PHS does not allow its usage in the automotive industry. To overcome this issue, PHS coils are produced with different metallic coatings, usually Al–Si (AS) or Zn-based (GI and GA), pre-applied in the steel rolling and coating plant. In the hot stamping process in an automobile factory, the metallic coating obtains its final structure and prevents the steel surface from decarburization [24]. Since Al–Si coatings offer only barrier protection and lack the ability of galvanic protection of the base steel in corrosive environments [64], they are not discussed in this review.

Coatings based on zinc are cheaper compared to Al–Si and offer both barrier and cathodic protection [65]. The formation of a complex Zn–Fe coating on PHS is divided into two steps. The first step is conventional hot-dip galvanizing of steel sheets in a bath of melted zinc with a minor addition of aluminum [66]. A typical GI hot-dip coating, as shown in Figure 2a, has a thickness of 10 µm and a coating weight per side of 70 $g \cdot m^{-2}$ [9,34,67,68]. The bath usually contains 0.2–0.5 wt.% of Al, which forms a thin layer of Fe_2Al_5 on top of the steel surface. It serves as a barrier between the steel and molten zinc, limiting the interdiffusion of the elements [69]. The addition of Al also increases the coating reflectivity [70]. Before the sheet is coiled, an optional step of annealing can be performed, resulting in galvannealed (GA) coated steel. Annealing leads to the interdiffusion of Zn and Fe atoms, forming a multiphase layered structure with a decreasing Fe gradient from the steel to the coating surface. The annealing causes an increase in the coating thickness. It is performed at 480–600 °C with a duration from seconds up to minutes depending on temperature and the desired coating thickness [70–72].

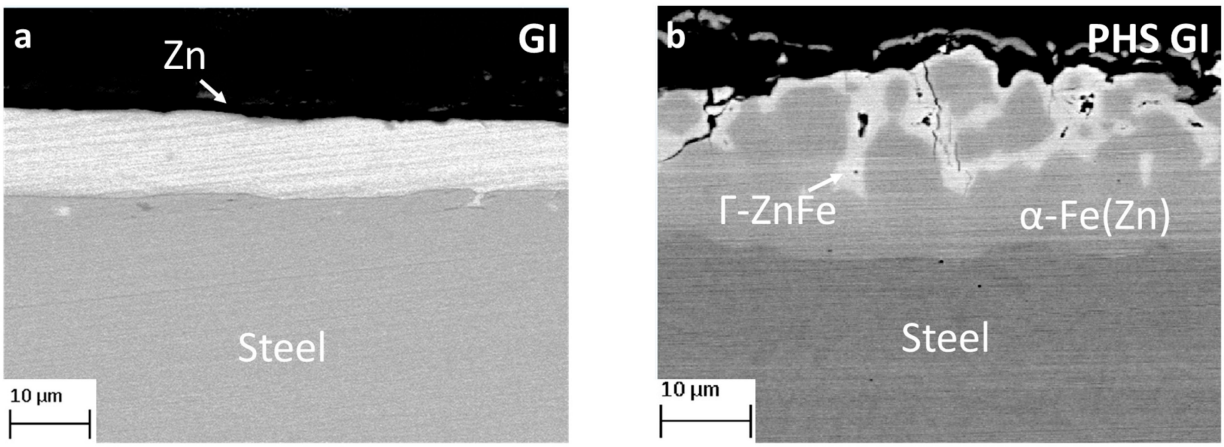

Figure 2. Steel with a GI coating before hot stamping (**a**) and a hot-stamped PHS GI (**b**).

If the galvannealing step is not performed, the final structure of the coating is obtained during the austenitization by interdiffusion of Zn and Fe. The interdiffusion is controlled by the layer of Fe_2Al_5 at the interface of zinc and steel [69]. The final PHS GI coating is 19–26 µm thick, and it is usually composed of Γ-ZnFe and zinc-saturated α-Fe, the α-Fe(Zn) phase (see Figure 2b). In the PHS GI coating, the Fe content in the α-Fe(Zn) phase is usually around 65 wt.%, and the Fe content in the Γ-ZnFe phase is approximately 20 wt.%. The phases are listed in Table 3 [68,69,73–76].

Table 3. Phases present in PHS GI and PHS GA coatings. Chemical formulas adapted from Ref. [74].

Phase	Chemical Formula	Fe Content [wt.%]
α-Fe(Zn)	Fe(Zn)	60–80 [70,77]
Γ-ZnFe	Fe_3Zn_{10}	11–24 [69]
δ-ZnFe	$FeZn_{10}$	7–14 [45,78]

The formation of Zn–Fe phases during austenitization depends on the dwell time and annealing temperature. As the dwell time increases, the phases evolve according to Equation (1), following the phase diagram shown in Figure 3 [45].

$$\eta\text{-Zn} \rightarrow \delta\text{-ZnFe} + \Gamma\text{-ZnFe} \rightarrow \Gamma\text{-ZnFe} + \alpha\text{-Fe(Zn)} \rightarrow \alpha\text{-Fe(Zn)} \quad (1)$$

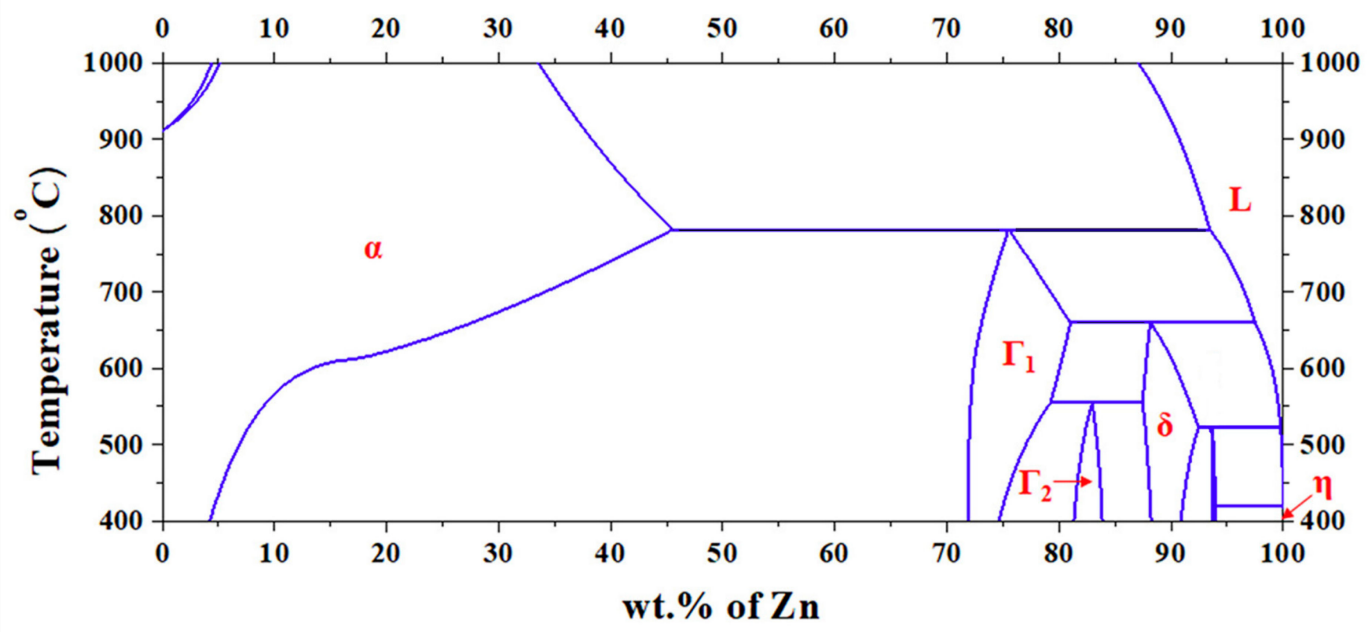

Figure 3. Binary phase diagram of Zn–Fe. Reprinted with permission from Ref. [79]. 2020, Elsevier.

As a metal sheet is inserted into the furnace, its temperature rapidly increases. A too-high heating rate can cause the Kirkendall effect, which is caused by the different diffusion rates of Zn and Fe, resulting in the formation of Kirkendall voids in the coating and the potential destruction of the coating [80]. When the coating–steel interface is heated to 460 °C, local decomposition of the Fe_2Al_5 layer occurs. At this point, zinc at the surface is in a liquid state. Released Al diffuses towards the surface and forms Al_2O_3 [81]. The rapid diffusion of Fe atoms into the coating occurs at temperatures above 500–550 °C, as observed by Kondratiuk et al. and Autengruber et al. [45,73]. At 550 °C, a larger part of zinc is enriched with iron, resulting in the formation of δ-ZnFe. At over 600 °C, the enrichment of Zn proceeds, and δ-ZnFe starts transforming into Γ-ZnFe [82]. At 700 °C, the transformation to Γ-ZnFe is almost complete. At this point, the interfacial Al layer completely dissolves, allowing for full diffusion of Fe from the steel. With a further increase in temperature over 780 °C, the formation of α-Fe(Zn) becomes dominant. Full transformation to α-Fe(Zn) is observed at temperatures above 880 °C [45,82,83]. As a result of interdiffusion and Fe enrichment, the melting point of the Zn–Fe binary solution increases, reaching 800 °C at 59 wt.% Fe. Temperatures above 930 °C cause increased evaporation of Zn from the outer layer of the coating. This results in decreased coating thickness and a damaged coating structure. In comparison with lower temperatures, there is also an increased amount of Fe_2O_3 forming on the surface due to the increased diffusion rate of Fe. More severe oxidation of Zn was also observed. At a temperature of 900 °C, full transformation to

the α-Fe(Zn) phase takes 4 min. Austenitization with a full α-Fe(Zn) transformation is not desired because it negatively impacts corrosion resistance and the cathodic protection capabilities of the coating [80].

Up to 700 °C, the PHS GI coating can contain η-Zn on the surface as the result of inhomogeneous diffusion of Fe. It takes approximately 2 min at temperatures over 700 °C to fully transform η-Zn into δ-ZnFe and Γ-ZnFe. At temperatures above 782 °C, the Zn-rich phases become liquid. The residual amount of melt on the surface in the austenitized state will change into Γ-ZnFe as a result of a peritectic reaction at 782 °C in the process of quenching. Differences in the composition of the enriched coating and liquid Zn with low Fe content are enhanced by the formation of microvoids and microcracks due to the Kirkendall effect. The evolution of the phases during annealing is shown in Figure 4 [45,80].

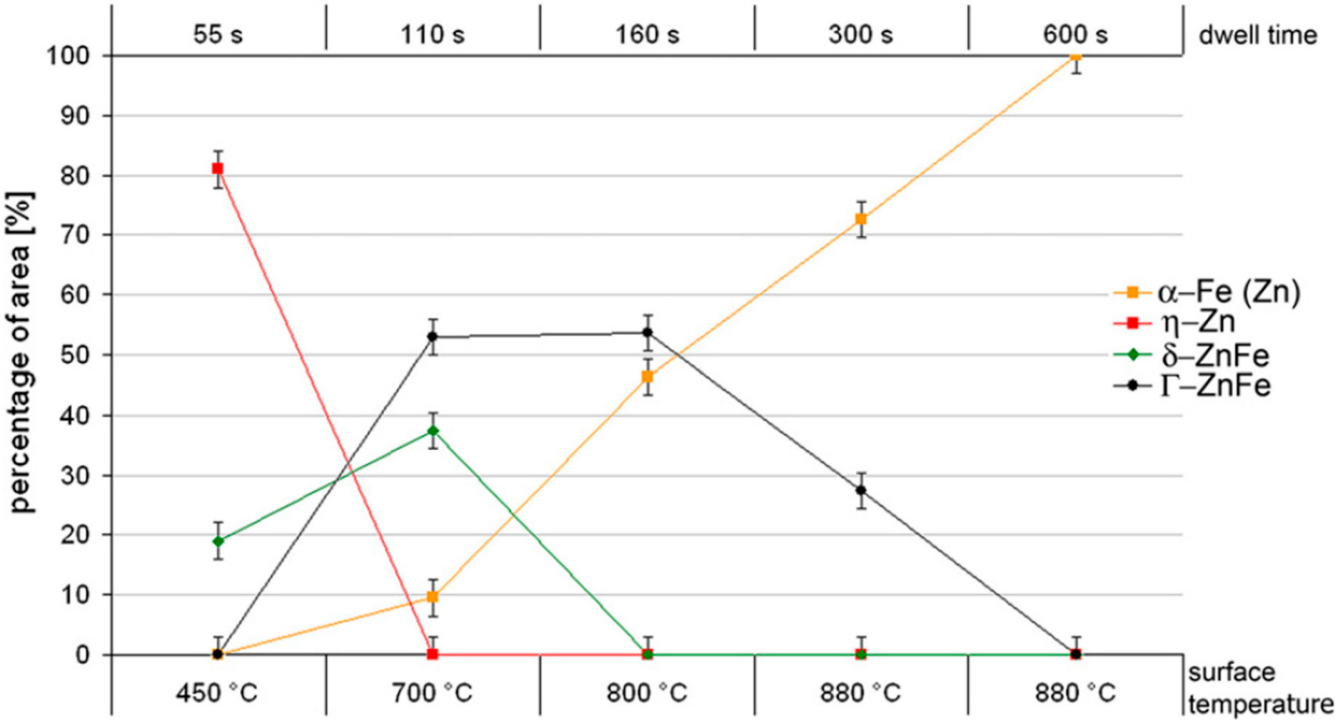

Figure 4. Evolution of the phases of hot-dip zinc coating as a function of time and temperature (surface temperature of a 1.5 mm-thick sheet; electrical chamber furnace heated to 880 °C). Reprinted with permission from Ref. [45]. 2011, Elsevier.

In the interval of austenitization temperatures ranging from 880 °C to 930 °C, α-Fe(Zn) is the stable phase [19,84]. Despite that, a small amount of non-reacted η-Zn phase can be present between the Fe-rich globular dendrites. When steel is rapidly heated or deformed and liquid Zn comes into contact with the steel surface, there is a risk of liquid metal embrittlement (LME), which is not desired and leads to deterioration of the mechanical properties of coated steel [81,82,85]. In the final PHS GI coating, the common phases are only Γ-ZnFe and α-Fe(Zn), and their ratio depends on the annealing conditions. The correct setting of time and temperature for austenitization, which ensures the desired parameters of coating, is shown in Figure 5 [86].

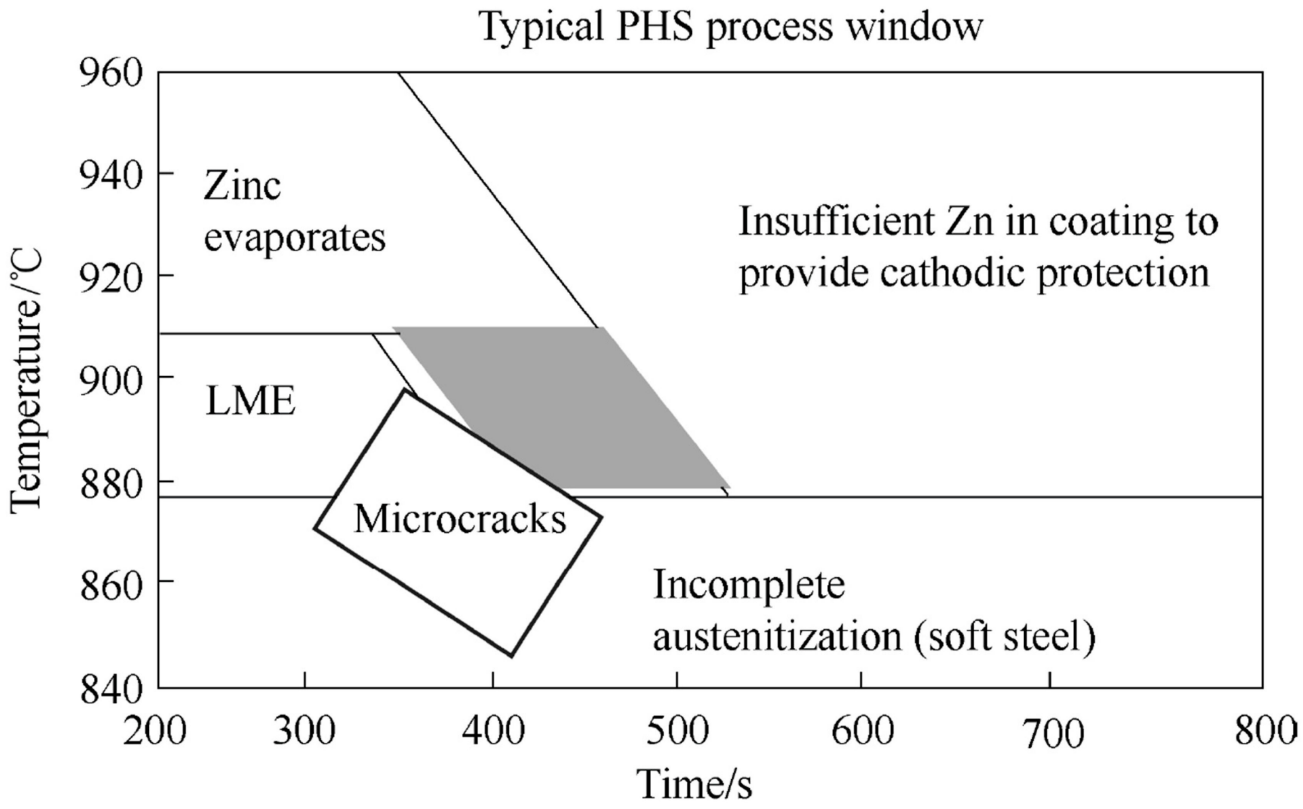

Figure 5. Typical setting of the PHS GI austenitization time and temperature (the gray area marks the correct parameters). Reprinted with permission from Ref. [86]. 2013, Goodwin, E.F.

3.2. PHS GI Structural Features and Defects

The phases typically present in the fully processed PHS GI, Γ-ZnFe and α-Fe(Zn), can provide cathodic protection of the base steel [73]. The cathodic protection ability of the coating depends on the ratio of the phases. With a longer annealing time, the content of Γ-ZnFe decreases and the content of α-Fe(Zn) increases. For robust cathodic protection, it is necessary that the coating contains 15 vol.% of Γ-ZnFe at minimum. A lower ratio of this zinc-rich phase reduces the cathodic protection provided by the coating by eliminating galvanic coupling between the two phases and by increasing the open circuit potential (OCP) of the coating [25].

Structural defects such as cracks and holes decrease the corrosion resistance of PHS GI as they allow for contact between the steel and the corrosive environment. As Drillet et al. stated, there may be occasional deep macrocracks occurring on the external bend radius of a hot stamped part [87]. More typical microcracks initiate as a result of friction and thermal expansion during hot stamping. In the heated state, thermal expansion of the coating is higher than for steel, 30.2×10^{-6} and 11.8×10^{-6} K, respectively. During the cooling process, shrinkage of the coating is more significant, and tensile stress responsible for the formation of microcracks is introduced into the coating layer. Microcracks are usually 10–12 μm deep but can go up to 50 μm. The propagation in the martensitic structure is not possible, and they mostly end at the coating–steel interface, as shown in Figure 6 [80,87].

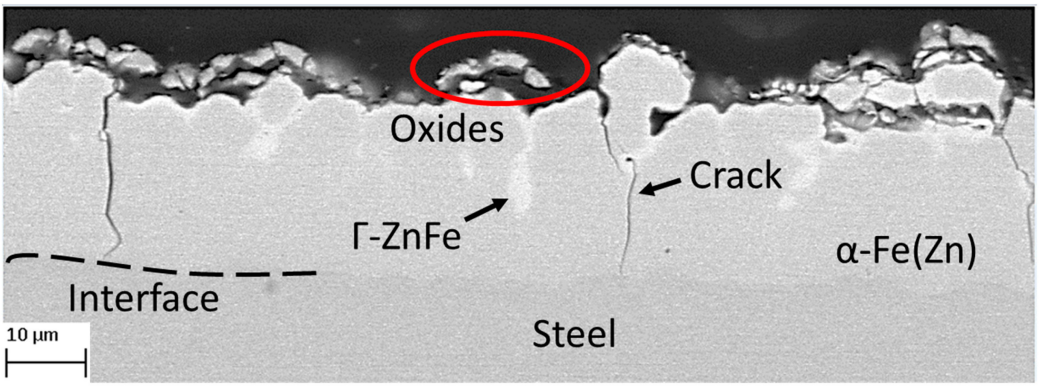

Figure 6. Structure of the PHS GI coating after hot stamping. Red circle marks oxides.

Intensive oxidation of the surface occurs during the austenitization. The formation of a liquid phase proceeds at a temperature of 648 °C, increasing the oxidation rate. The solid oxidic layer on the surface protects the metallic zinc from further oxidation [73]. The layer of oxides is approximately 0.8–2.5 µm thick, and this thickness may strongly differ. Longer annealing time leads to excessive formation of Fe_2O_3 on the top. Oxides contain many defects that tend to merge and create spherical structures with ravine-like morphology. The structure and amount of oxides become stable at austenitization times over 480 s [84,88]. The corrosion resistance of the coating increases with the quantity of oxides [25].

ZnO is the dominant surface oxide on PHS GI. Other oxides are $ZnAl_2O_4$, Al_2O_3, and $(Mn,Zn)Mn_2O_4$. Oxides of Mn and Al are present due to the diffusion of these elements from the coating–steel interface to the surface during the austenitization process. The share of Mn oxides is 4 wt.%, and their spinel structure can contain atoms of Fe as substituents. A notable amount of Cr from the steel was also detected in the oxide layer of $ZnAl_2O_4$ [83,84,88,89].

Lee et al. stated that the Al_2O_3 formed during the hot stamping at the surface works as a barrier, preventing evaporation and oxidation of the liquid zinc [82]. During cooldown and solidification, material contraction occurs, and the surface morphology changes into rougher structures. A coherent layer of Al_2O_3 cracks, resulting in the oxidation of the underlying Zn and Mn. Oxides of Zn and Mn cover the damaged layer of Al oxides in the final structure, but islands of Al_2O_3 can still be observed on the surface. Faster heating rates enhance the integrity of the Al oxide film. At the heating rate of 10 $K{\cdot}s^{-1}$, a thin liquid layer of zinc remains on the surface, allowing for uniform distribution of Al on the top. After cooling down, the surface is smoother and covered with a layer of Al_2O_3. If present in a sufficient amount, Cr from the steel can supplement Al and repair the protective layer in the form of Cr_2O_3 [83].

4. Hydrogen Embrittlement of PHS

4.1. Hydrogen Embrittlement

The phenomenon of HE, which is responsible for the change in ductile fracture to brittle, is caused by diffusible hydrogen present in the metal lattice. Diffusible hydrogen is non-trapped or temporarily trapped atomic hydrogen, which can move freely in the steel matrix and interact with defects. The fact that diffusible hydrogen can move freely means that its concentration may significantly vary depending on actual exposure conditions. Although the mechanism of the interaction between the metal lattice and atomic hydrogen has been described by numerous theories, most of them were confirmed only for certain materials and conditions. In real scenarios, a combination of the mechanisms is needed to describe the fracture behavior of PHS [90]. A detailed description of the HE mechanisms is not the focus of this review, as it can be found elsewhere [91,92].

4.2. Hydrogen Formation and Absorption

The evolution of the diffusible hydrogen content in PHS over time is shown schematically in Figure 7. During the manufacturing process of PHS parts, hydrogen is introduced by contact of a hot steel sheet with air humidity [93]. A significant amount of hydrogen can also enter the steel during the welding process. The thermal decomposition of water molecules or impurities such as cleaning oil and other organic compounds on the surface can substantially increase the overall quantity of hydrogen present in the material [94]. Other operations that cause hydrogen absorption are chemical treatments, including cleaning and painting [30,95]. The hydrogen absorbed during these processes is commonly eliminated by paint baking at 200 °C [61,96,97].

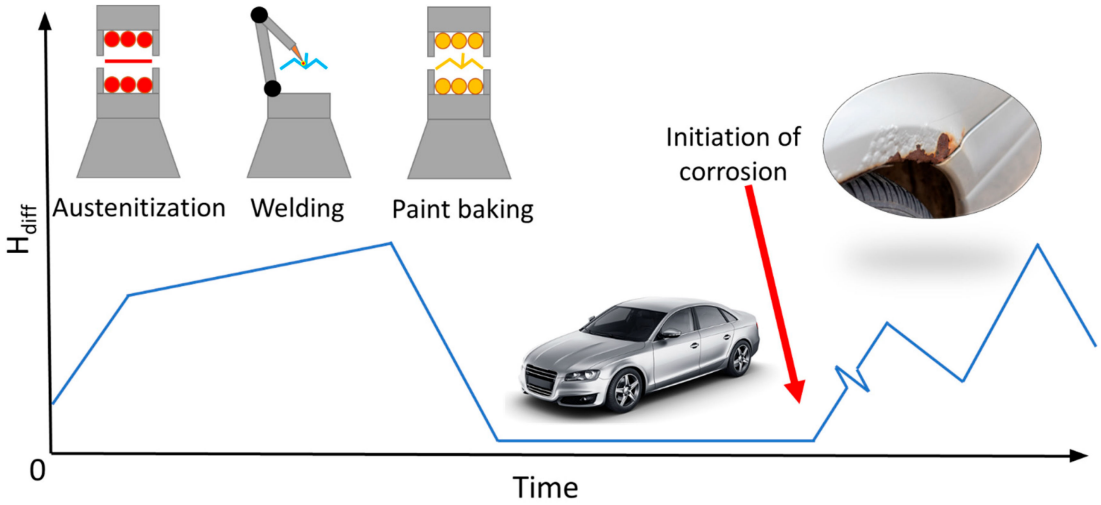

Figure 7. Time dependency of diffusible hydrogen content in PHS car parts.

In the car service life, hydrogen uptake can be caused by the corrosion of steel components. The concentration of corrosion-induced hydrogen in the steel strongly depends on exposure conditions, steel corrosion rate, steel polarization in defects by sacrificial coatings, and other parameters [98]. Automobiles are exposed to various corrosive environments ranging from dry deserts to the extremely humid environments of rainforests. For different periods, a car body is in contact with air humidity, which causes the formation of a thin layer of surface electrolyte and eventually the initiation of corrosion reactions. Separating anodic and cathodic sites leads to a non-uniform pH distribution on the surface. Local acidification occurs at anodic sites where steel is oxidized by Equation (2). At cathodic sites, the hydrogen evolution reaction (HER) by Equation (3) and the oxygen reduction reaction (ORR) by Equation (4) can occur. On steel, the reaction rate of the ORR is generally higher compared to the HER [99].

$$Fe \rightarrow Fe^{2+} + 2e^{-} \quad (2)$$

$$2H^{+} + 2e^{-} \rightarrow H_2 \quad (3)$$

$$O_2 + 2H_2O + 4e^{-} \rightarrow 4OH^{-} \quad (4)$$

The process of hydrogen absorption is described by Volmer–Tafel–Heyrovsky reactions. The Volmer reaction, Equation (5), describes the cathodic reduction in hydrogen ions with subsequent adsorption of hydrogen to the metal surface (MH_{ads}). In competition with the Volmer reaction, chemical desorption of molecular hydrogen is realized by reactions of Tafel, Equation (6), and Heyrovsky, Equation (7). Simultaneously with these reactions, some adsorbed hydrogen may be absorbed into the material, following Equation (8) [31,100].

$$H^{+} + M + e^{-} \rightarrow MH_{ads} \quad (5)$$

$$2MH_{ads} \rightarrow H_2 + 2M \quad (6)$$

$$MH_{ads} + H^+ + e^- \rightarrow M + H_2 \quad (7)$$

$$MH_{ads} \rightarrow MH_{abs} \quad (8)$$

In the case of atmospheric corrosion of bare steel, the rapid formation of a layer of corrosion products widely known as red rust occurs. Its formation is characterized by multiple reactions of hydrolysis of iron ions (Equations (9)–(11)) and is responsible for hydrogen ion production, which decreases the surface pH and leads to the promotion of the HER and hydrogen content in the material [101,102].

$$Fe^{2+} + 2H_2O \rightarrow 4Fe(OH)_2 + 2H^+ \quad (9)$$

$$4Fe^{2+} + O_2 + 6H_2O \rightarrow 4FeOOH + 8H^+ \quad (10)$$

$$Fe^{3+} + 3H_2O \rightarrow Fe(OH)_3 + 3H^+ \quad (11)$$

Hydrogen entry under atmospheric conditions is connected to the existence of a thin film of liquid on the surface of exposed steel. The corrosion rate evolves continuously due to changes in temperature, humidity, electrolyte composition, and the amount of corrosion products and their speciation. The corrosion rate is controlled mainly by the ORR, which depends on the rate of oxygen diffusion to the surface. With the decrease in electrolyte thickness to 100 µm, the rate of reaction can be 3–4 times higher compared to steel immersed in bulk electrolyte because of a better oxygen supply [103]. Stratmann et al. measured the highest corrosion rate at the electrolyte thickness of 10 µm, which can be formed during drying [104,105]. In general, a decrease in the electrolyte film thickness moves the cathodic reactions towards noble values, suggesting an increase in oxygen reduction efficiency [103]. With further decrease in the electrolyte thickness under 10 µm, the oxygen solubility decreases as a result of increasing concentration of ions dissolved in liquid [104]. Since the ORR competes with the reduction and absorption of hydrogen ions, thick acidic electrolytes with a low oxygen concentration will favor hydrogen uptake [106]. Except for crevices, these conditions are not common in automotive applications for prolonged periods. In atmospheric conditions with NaCl contamination, the hydrogen absorption rate monitored by a hydrogen permeation test increased from 40% RH to reach the highest value at 74% RH [107]. Following the Kelvin equation, Haruna et al. proposed that NaCl solids trapped in red rust create small saturated droplets, which increase in diameter and cover larger areas with increasing RH [107].

The rate of the HER during atmospheric corrosion strongly depends on exposure conditions. The amount of hydrogen in steel can rapidly change following wet/dry cycling [108]. A ratio of the HER and ORR continuing on the surface of chloride-contaminated bare PHS corroding in atmospheric conditions was investigated by Machackova et al. [99]. The results of the respirometry investigation showed that the HER was responsible for 17% of the cathodic charge transfer for bare PHS. The HER was initiated immediately after the start of exposure to air at 85% RH. After an initial decrease, it stayed relatively stable at 14% during a 5-day exposure. Rudomilova et al. showed the importance of the surface pH distribution [28]. A thin electrolyte film favors the separation of anodic and cathodic regions. Acidic conditions in anodic regions favor the uptake of hydrogen produced from H^+ formed by the hydrolysis of iron ions [101,107]. When a layer of corrosion products is formed, further growth of the layer facilitates hydrogen production due to acidification of the inner corrosion products [109]. In the case of contamination by NaCl, the pH value beneath a layer of corrosion products can drop to a range from 4.2 to 4.3 [107]. The formation of pits is possible in the presence of iron–chloride complexes. With progressing corrosion, the pits become enclosed with a rust cap, as seen in Figure 8. An anodic area is

established at the tip of the pit, supplying Fe ions to the rust cap. The surface under the cap and the pit sides act as a cathode with limited access to oxygen. The effect of a small anodic area causing strong hydrogen uptake to AHSS was also confirmed by Nazarov et al. [110]. When the concentration of oxygen inside the pit becomes low, the HER and the Fe^{3+} ion reduction described by Equation (12) gain importance [99,111]. The partial transformation of lepidocrocite into magnetite proceeds according to Equation (13) along with the hydrolysis of Fe^{2+} ions in Equation (9), contributing to the evolution of hydrogen [112]. As a result of iron hydrolysis, the pH can decrease to 3 or less. An analogical effect on the rust cap can be provided by a salt crust. In this case, the composition and concentration of salt directly affect the formation of corrosion products and H entry [113].

$$Fe^{3+} + e^- \rightarrow Fe^{2+} \quad (12)$$

$$Fe^{2+} + 2\gamma - FeOOH \rightarrow Fe_3O_4 + 2H^+ \quad (13)$$

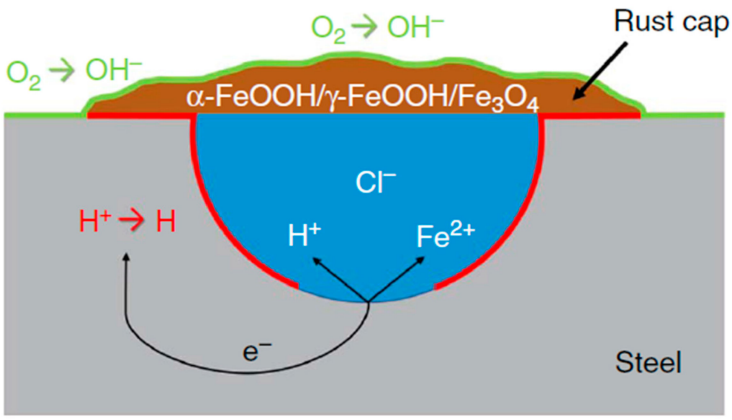

Figure 8. Schematics of the pit with a rust cap promoting the HER and hydrogen entry. Reprinted with permission from Ref. [28]. 2021, National Association of Corrosion.

The concentration of hydrogen in the metal is the highest near the surface and becomes lower in the direction of bulk [114,115]. The diffusion of hydrogen atoms is driven by the concentration gradient [116]. The diffusion coefficient of hydrogen in bare PHS is approximately 4.5×10^{-7} $cm^2 \cdot s^{-1}$ [117]. Hydrogen atoms diffuse through bcc tetrahedral or fcc octahedral interstitial sites and are drawn towards defects of the crystal lattice, which hinder their movement [118]. These sites are known as traps [31].

4.3. Hydrogen Traps

Traps represented by dislocations, vacancies, solute atoms, inclusions, and grain boundaries are defects of the crystal lattice, which can be divided into sinks and sources based on the interaction with hydrogen. If a trap catches a hydrogen atom and hinders its movement, it acts as a sink. A high number of sinks in steel is desired because they decrease the content of diffusible hydrogen and suppress the risk of HE. Under certain circumstances, hydrogen can be released from a trap, which then acts as the hydrogen source. Traps can be divided based on their binding energy, which describes the ability to release hydrogen. Traps with a high binding energy, also known as irreversible, do not release hydrogen atoms to the lattice once trapped. For the release of hydrogen, high temperatures are necessary. Atoms bonded in these traps do not significantly contribute to HE. Low-energy reversible traps can catch and release hydrogen atoms depending on the temperature. The binding energy of reversible traps does not exceed 60 $kJ \cdot mol^{-1}$ [119,120]. They have a crucial impact on the transport of hydrogen in the material and HE [116]. Reversible traps can have a variety of energy ranges, including 0–20 $kJ \cdot mol^{-1}$ for the elastic stress field of dislocation, 20–40 $kJ \cdot mol^{-1}$ for the core of screw dislocation or grain

boundary, and 49–55 kJ·mol^{-1} for high angle grain boundaries [121]. High-energy traps can attract hydrogen from weaker traps and act as sinks [91,122–124].

Dislocations are one of the most common reversible lattice defects that interact with hydrogen; they tend to accumulate in the vicinity of the elastic stress core of the dislocation. Hydrogen atoms in low concentration levels can increase dislocation mobility and soften the material. In high concentrations, hydrogen can form atmospheres and create drag forces, which leads to a change in the dislocation slip of the steel and material hardening [125]. For PHS, dislocation density calculated with the mathematic model of Jo et al. is 2.21 $\times$ 10^{15} m^{-2} [126]. This value is close to the dislocation density of 1.42 $\times$ 10^{15} m^{-2} measured for Fe—0.4 wt.% C martensitic steel.

In general, grain boundaries can irreversibly trap large amounts of hydrogen, improving the HE resistance [127]. To increase the volume fraction of grain boundaries, PAG refinement and subsequent refinement of martensitic packets, blocks, and laths can be achieved by adding 0.05 wt.% Nb or V [32,125,128]. PAG size affects the hydrogen diffusion coefficient in the material. Research by Li et al. showed that a decrease in the PAG size from 22 to 14 µm resulted in a 10% lower hydrogen diffusion coefficient [129]. This phenomenon was attributed to a combination of two effects linked to the grain boundaries of previously mentioned substructures of PAGs. Firstly, finer grains lead to an increased unit volume of grain boundaries, which can act as a path for hydrogen diffusion. This would lead to a higher diffusion coefficient. In contrast, the trapping effect of boundaries between grains/packets/blocks/laths and triple junctions of grains goes against boundary diffusivity and is more significant. As a result, materials with finer PAGs tend to absorb more hydrogen, which becomes permanently trapped and does not contribute to HE. Latypova et al. described how the elongation of PAGs led to a slow quasi-cleavage fracture, whereas an equiaxed PAG structure was prone to intergranular cracks [130].

In PHS, carbides of Mo, V, Ni, and Nb can rapidly decrease susceptibility to HE by decreasing the diffusion rate of hydrogen in the metal lattice. Vanadium carbides (V_4C_3) can hinder hydrogen-induced delayed fracture [124]. Alloying with 0.05 wt.% of Ti or Nb leads to the formation of elliptical carbides with the size of 5 nm, which are homogeneously distributed. The presence of these carbides retards hydrogen diffusion and makes PHS more resistant against HE despite having a higher diffusible hydrogen content [131]. Elements such as S, P, Sb, and Sn may increase the susceptibility of steel to HE. These impurities tend to segregate on grain boundaries and enhance intergranular cracking [125,132,133]. The effect of MnS on HE depends on the morphology of inclusions. It forms soft inclusions with high H-trapping energy. When they are finely dispersed and smaller than 1 µm, HE is suppressed. In contrast, coarse elongated inclusions cause higher susceptibility to HE [134].

Retained austenite is found in PHS after quenching at 0 to 7.1 vol.%. In commonly used PHS, the content of retained austenite is quite low, but recent studies show that a higher content of stable RA leads to an increase in ductility without compromising the UTS. To increase the volume of RA, higher temperatures and lower pressure quenching dies are necessary [20,51,92]. The fcc structure of austenite has low diffusivity and high solubility of hydrogen; therefore, RA acts as a stronger hydrogen trap compared to dislocations or grain boundaries. Hydrogen content in austenite can be three times higher than in martensite [135]. In a corrosive environment, RA has a beneficial effect on HE since it can absorb excessive hydrogen from the martensitic lattice and immobilize it. RA grains with a size under 200 nm in the martensitic PHS structure changed the hydrogen diffusion coefficient from 5.97 $\times$ 10^{-7} to 3.83 $\times$ 10^{-7} cm^2·s^{-1} [136]. Malitckii et al. and Chan et al. stated that hydrogen in PHS with RA is mostly trapped at the interface between filmy RA and the martensitic matrix, as shown in Figure 9 [137,138].

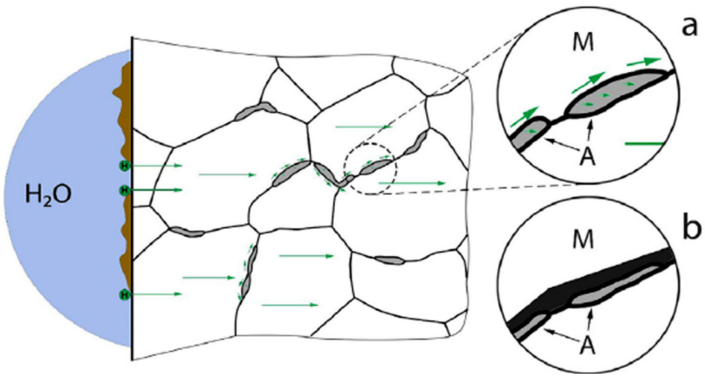

Figure 9. Hydrogen flow within the martensitic steel interacting with filmy retained austenite (gray zones). (**a**) hydrogen uptake and diffusion. (**b**) intergranular fracture. Reprinted from Ref. [137].

5. Corrosion Properties of PHS GI

The hot stamping process affects the corrosion resistance of PHS GI by changing the electrochemical properties of the coating and its thickness. The GI coating in the solution of 100 g·L^{-1} $ZnSO_4 \cdot 7H_2O$ and 200 g·L^{-1} NaCl against the Pt electrode exhibits an E_{corr} of −0.76 V/SHE. Intermetallic phases formed on PHS GI, Γ-ZnFe and α-Fe(Zn), have more noble potential (−0.54 and −0.40 V/SHE, respectively). When exposed to a corrosive environment, the Γ-ZnFe phase acts as anode and corrodes preferentially, protecting the α-Fe(Zn) phase. After depletion of the Γ-ZnFe phase, corrosion of the α-Fe(Zn) phase takes place. If a defect in the remaining coating appears, α-Fe(Zn) acts as anode and galvanic protection of the exposed steel with an E_{corr} of −0.22 V/SHE occurs [9,25]. This mechanism generally works, but α-Fe(Zn) can start corroding locally while Γ-ZnFe is still present in a different area [139]. The contact of steel with the corrosive environment is realized in through-coating cracks, which means that galvanic couple α-Fe(Zn)–steel is activated sooner than may be anticipated. To ensure cathodic protection, the minimal content of Zn in the α-Fe(Zn) phase should be above 10 wt.% [70]. In comparison with a conventional GI coating, the lower potential difference between the phases in PHS GI and steel leads to lower polarization of the coating, resulting in its lower corrosion rate. This was confirmed by Dosdat et al. in a 15-week atmospheric corrosion test, VDA 621–415, where PHS GI outperformed steel with a GI coating and bare steel four and six times, respectively [26]. Even a higher difference was found for mean pit depth, which was 20, 120, and 340 µm for the respective materials.

The composition of corrosion products strongly affects the corrosion resistance of PHS GI. The presence of Zn–Fe intermetallics causes the formation of different types of corrosion products. During the corrosion of Γ-ZnFe in an environment containing NaCl, the detected stable corrosion products were akaganeite β-FeOOH, hydrozincite $Zn_5(CO_3)_2(OH)_6$, and simonkolleite $Zn_5(OH)_8Cl_2 \cdot H_2O$ [9]. Corrosion products of Zn originated in the initial phase of corrosion as ZnO formed by hydrolysis of Zn^{2+} ions. Alongside Zn-based corrosion products, oxides of Al in various forms and Mn-based oxides, originating from hot stamping, were also confirmed [140]. With prolonged exposure, ZnO in cathodic areas is transformed into hydrozincite. For this reaction, alkali conditions and good access to CO_2 are needed. A high concentration of chlorides at anodic sites allows for the formation of simonkolleite, which reduces the corrosion rate. This feature of simonkolleite is provided by the ability to bond chloride ions, low solubility, low electron transfer ability, and a dense structure, which together result in a good ability to block the transport of species to the corroding surface [139,141,142]. Increased annealing time leads to an increased volume of α-Fe(Zn), which in an environment with a high concentration of chloride ions supports the formation of akaganeite. This effect is visible mostly after 200 s of annealing at 900 °C. Akaganeite is a polymorph ferric oxyhydroxide with a low amount of bonded chloride with the chemical formula $FeO_{0.833}(OH)_{1.167}Cl_{0.167}$. It is observed at anodic sites with simonkolleite [99]. A decrease in Γ-ZnFe under 15 vol.% led

to a three times higher mass gain in atmospheric corrosion tests [25]. Simonkolleite and akageneite were mainly formed during the dry phase of exposure after the concentration of chlorides in the surface solution had increased [9]. In cathodic areas where Al_2O_3 is present, contamination with NaCl allows for the formation of dawsonite $NaAlCO_3(OH)_2$ in the initial phases of corrosion. Directly after exposure to a high concentration of SO_4^{2-}, the formation of gordaite $Zn_4Na(OH)_6(SO_4)Cl{\cdot}H_2O$ and lahnsteinite $Zn_4(SO_4)(OH)_6{\cdot}3H_2O$ takes place. These corrosion products offer good barrier protection, which can cause up to a 60% decrease in mass loss [139].

During corrosion, hydrogen may be introduced to PHS GI as a result of electrochemical processes on the surface. At first, the coating phases may create galvanic couples and start corroding. The formation of an additional galvanic couple involving steel and the coating phases occurs either because of the presence of cracks or the formation of through-coating corrosion defects. The effect of galvanic coupling leads to cathodic polarization of α-Fe(Zn) and steel, where subsequent hydrogen evolution occurs. The coating acts as a sacrificial anode, corroding by Equations (2) and (14). At cathodic sites, the oxygen reduction reaction (Equation (4)) and hydrogen evolution reaction (Equation (3)) take place [25,143]. For PHS GI at 85% RH at 35 °C contaminated with 0.9 $g{\cdot}m^{-2}$ NaCl in methanol, the HER represented an average of 12% of the cathodic process. The highest rate and ratio of the HER of 24% was measured during the first 8 h of exposure. The HER significantly slowed down after 24 h, and its share in the cathodic process was approximately 7%. The decrease was connected with the formation of stable corrosion products, which blocked cracks and defects in the coating [99].

$$Zn \rightarrow Zn^{2+} + 2e^{-} \quad (14)$$

6. Risk of HE of PHS

6.1. Non-Coated PHS

HE of the PHS depends on the content of diffusible hydrogen present in the steel matrix in combination with its structural features, which are given by the composition and manufacturing process. This section focuses on the fracture behavior of PHS, the critical hydrogen content causing failure of the material, and the influence of microstructural features on HE.

When evaluating the fracture behavior of PHS, it is essential to consider all factors that may lead to the deterioration of the mechanical properties of the tested material. These factors include temperature, surface condition, and reduction in the cross-section area. In corrosive environments, the cross-section area reduction can occur due to the formation of pits or uniform corrosion. It can cause a drop in the UTS or elongation that can be incorrectly assigned to HE [144]. It is therefore crucial to separate the effect of corrosion and the presence of hydrogen in experiments.

The nature of diffusible hydrogen is in a kind of dynamic equilibrium with the environment, influenced by the conditions of exposure or artificial charging. The concentration may vary in a matter of minutes or a few hours and in combination with other factors such as the structure of the steel and its hydrogen retention capabilities; the whole system has multiple variables influencing the fracture mechanics. With increasing hydrogen content, the strength of the steel decreases. This decrease may be reversible, especially for steels with low hydrogen content, where the restoration of tensile strength may be realized within several hours after removal from the charging environment [145]. The effects of hydrogen may be evaluated by loss of the UTS and ductility or changes in the morphology of the fracture surface. Hydrogen-free steel provides the highest UTS and ductility. The fracture morphology exhibits small dimples typical for a ductile fracture, as seen in Figure 10a. The fracture area can be divided into an area of shallow dimples near the surface of the fractured sample and an area of micro-void coalescence in the center created by plastic deformation and necking. With an increasing hydrogen content, the strength and ductility decrease. Fracture morphology changes to quasi-cleavage progressing transgranularly along (011) planes of martensitic laths, as seen in Figure 10b. With an even higher con-

tent of diffusible hydrogen, the strength further decreases and intergranular facets typical for embrittled material occur (Figure 10c). Necking near the fracture is minimal or non-visible [29,30,51,145,146]. Cracks initiate on the surface and propagate into the bulk with flat intergranular facets following PAGs or martensitic lath boundaries [147]. The depth of the intergranular fracture area depends on the content of hydrogen [148]. The brittle intergranular area can be limited to the vicinity of the surface by using Nb, which traps hydrogen and provides strengthening by dispersive carbides. Impurities in the steel can also cause the initiation of intergranular cracks [149,150]. The lamellar austenite–martensite structure is often the initiation site of cracks along the PAGs [151]. Intergranular fracture initiation can be caused by large PAGs, which allow for very high hydrogen concentration at their boundaries.

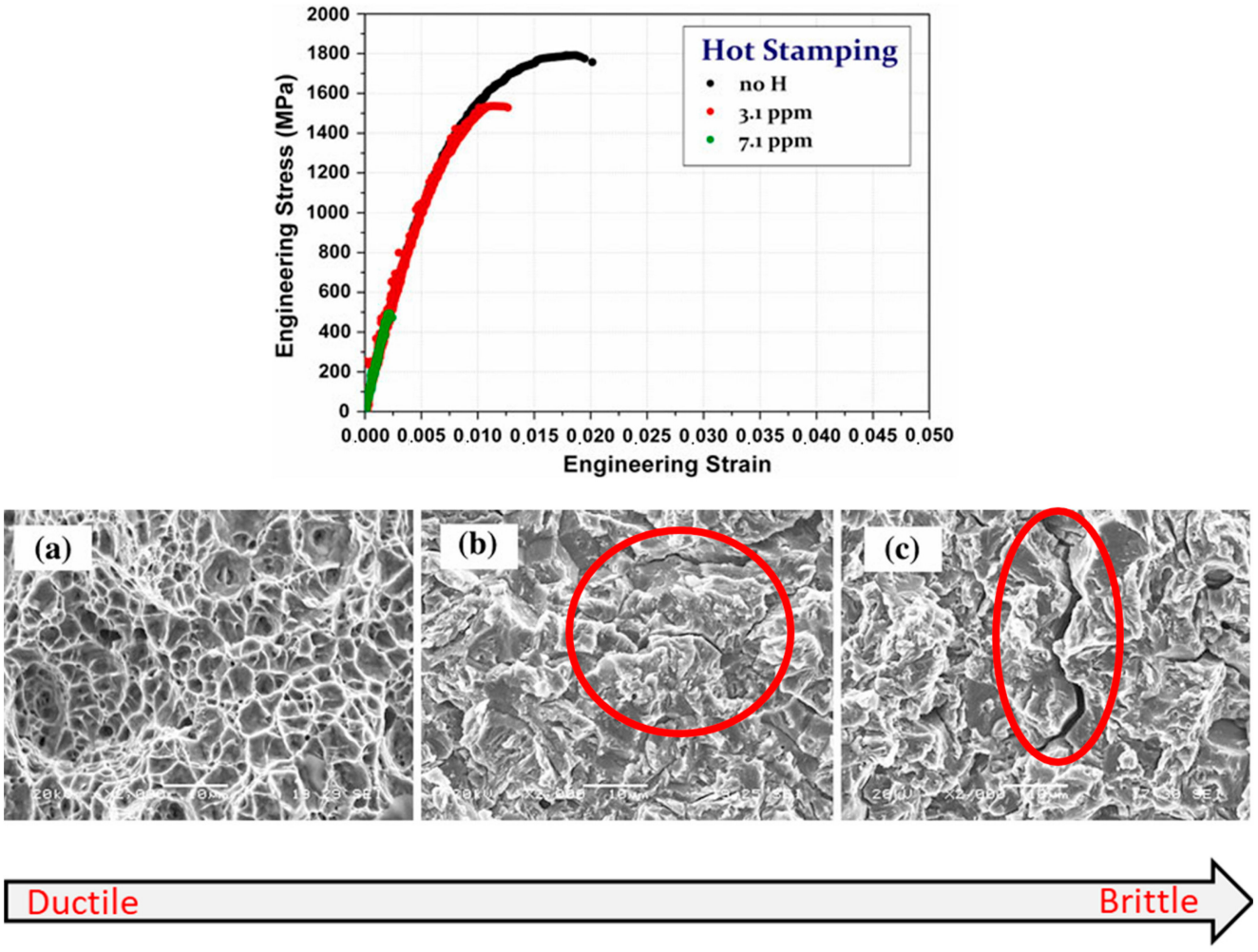

Figure 10. Stress–strain curves of PHS with a UTS of 1600 MPa as a function of total hydrogen content introduced by electrochemical charging prior to mechanical testing and corresponding fracture morphologies. Reprinted with permission from Ref. [30], 2012, Springer Nature: (**a**) ductile fracture, (**b**) quasi-cleavage fracture progressing transgranularly along (011) planes of martensitic laths, and (**c**) intergranular facets typical for embrittled material. Red circle marks specific feature of the fracture surface.

The concentration of diffusible hydrogen, which causes material failure, is known as the critical diffusible hydrogen content (H_C), and it is specific for different grades of PHS. For modern PHS with a high UTS, H_C can be as low as 1 ppm [30,31,152]. Lovicu et al. compared the mechanical properties of PHS with various hydrogen contents using the slow strain rate test (SSRT) [30]. The UTS decreased from 1800 MPa for non-charged steel to 450 MPa for steel with a total hydrogen content of 8.5 ppm. The most significant drop in UTS was observed from 4 ppm of the total hydrogen (see Figure 11a). A comparable degradation was observed by Lee et al. at 1.7 ppm of diffusible hydrogen [29]. The strength loss is specific for particular PHS grades, as demonstrated by Cao et al., who compared PHS grades with a UTS of 1500 MPa and 2000 MPa, respectively [147]. Steel sheets were austenitized, quenched, and tempered at 170 °C for 20 min to simulate the paint baking process. Samples were electrochemically charged in a solution of 3 wt.% NaCl and 0.3 wt.% NH_4SCN with a current density of 0.1 $mA \cdot cm^{-2}$. The results obtained by the SSRT showed that the UTS of the 2000 MPa steel decreased more rapidly than for the 1500 MPa steel, as seen in Figure 11b. This indicates a higher HE susceptibility of steels with a higher UTS. The studied steel grades had a comparable UTS at 0.5 ppm of diffusible hydrogen. The authors emphasized that exposure to a mildly corrosive environment should not result in surpassing this concentration. An intensive electrochemical charge reduced the UTS of the 2000 MPa steel below that of the 1500 MPa steel. The strength of the steels with a UTS of 1500 MPa or more, which are charged with higher hydrogen concentrations, usually plateaus, as pictured in Figure 11a,b [30,147]. Based on constant load test (CL) data, the failure probability of such parts with high hydrogen content may reach 20% at 70% of the UTS [147].

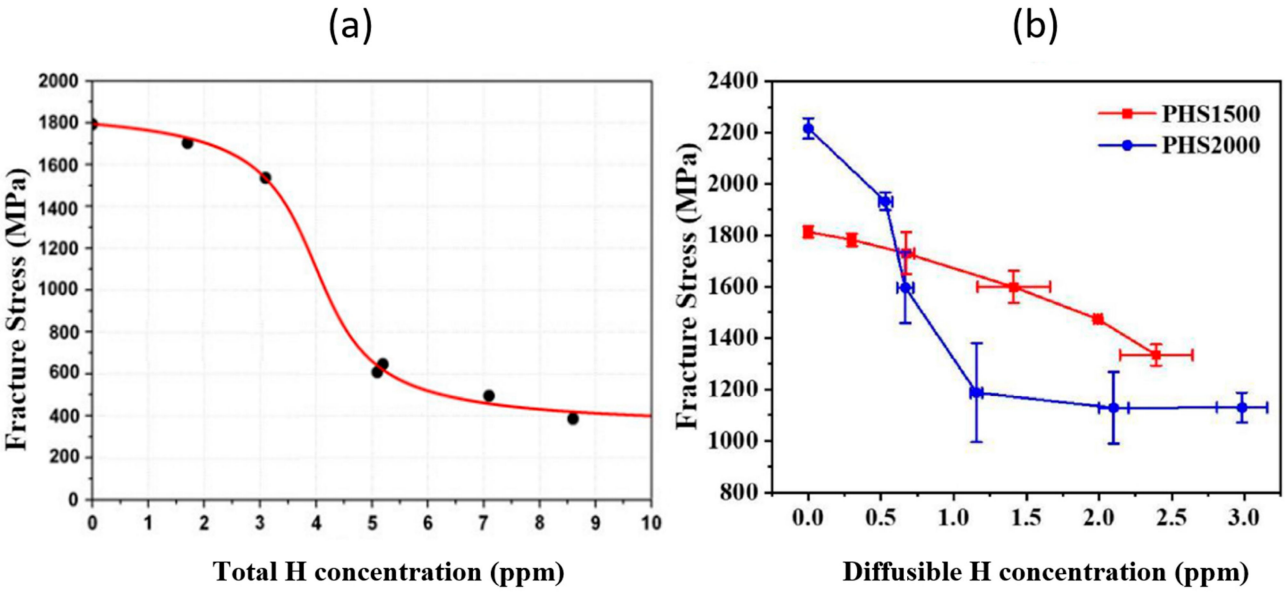

Figure 11. Loss of UTS as a function of total hydrogen content (**a**) (Reprinted with permission from Ref. [30], 2012, Springer Nature [30]) and diffusible hydrogen content (**b**). Reprinted with permission from Ref. [147]. 2022, Elsevier.

The transport of hydrogen in a martensitic matrix is closely tied to the introduction of hydrogen to the material and its desorption. Especially in an environment with changing wet/dry cycles, actual concentrations of diffusible hydrogen can rapidly change depending on the phase of the cycle [153]. Structural factors such as grain size and precipitates given by the manufacturing process have the main effect on the diffusion and trapping of hydrogen in the steel matrix, which consequently changes the mechanical properties [149,154,155]. Okayasu et al. compared samples austenitized at elevated temperatures of 920 °C and 1000 °C. The difference of 80 °C led to a nearly two-times larger PAG size [156]. This result

is comparable to that of Cao et al. [147]. The UTS and surface hardness of the samples were similar, but the diffusible hydrogen content after electrochemical charging was 0.8 and 0.9 ppm for samples austenitized at 920 °C and 1000 °C, respectively. The difference led to worse mechanical performance of the steel austenitized at the higher temperature. When comparing steels in a charged state, steel with a larger PAG achieved twice as bad CL and cyclical load test results [156]. The influence of the PAG size on hydrogen absorption was also confirmed by Ngiam et al. [157]. The PAG boundary concentrates stress and diffusible hydrogen, which can be 2.5 times higher than the bulk. Regions with high hydrogen concentrations act as initiation sites for intergranular fractures along PAG boundaries. The same effect was observed for martensite lath boundaries at the global concentrations of diffusible hydrogen above 1.5 ppm. At high hydrogen concentrations, the fracture mechanism can be both intergranular at PAG boundaries and transgranular along lath boundaries. Otherwise, the rest of the hydrogen was trapped in the matrix without causing critical stress leading to fracture initiation.

Mitigation of hydrogen diffusion can be achieved by carbides of Nb, Ti, and V. The hydrogen trapping effect of carbides was investigated by Wei et al., who reported that the effectivity of H trapping decreases in order NbC > TiC >> VC [158]. Compared to Nb, Ti carbides can trap H only at coherent or semicoherent interfaces with the steel matrix. Carbides of Nb provide the highest H trapping ability, decreasing the diffusion coefficient from 10.2×10^{-7} $cm^2 \cdot s^{-1}$ for a Nb-free PHS to 2.9×10^{-7} $cm^2 \cdot s^{-1}$ for PHS alloyed with a 0.053 wt.% of Nb [131]. This amount seemed to offer the best HE resistance, which was caused by grain refinement from 16.4 μm to 6.7 μm for the unalloyed PHS and Nb-alloyed PHS, respectively, and the ability of NbC to act as strong hydrogen traps. The Nb-alloying of 0.05 wt.% led to an increase in the UTS of hydrogen-charged material from 400 MPa to 1100 MPa. Microalloying with a combination of Nb, Ti, and V provides a synergic effect and leads to the formation of mixed carbides with a size of 12 nm [159]. The addition of 0.04 wt.% Nb and V to 22MnB5 steel allow the PHS to absorb two times more total hydrogen than unalloyed steel. Thanks to the permanent nature of the traps, this hydrogen does not hinder the mechanical performance of the steel, and the material benefits from the refinement of martensitic laths. A significant improvement of HE resistance was observed via bend test in 0.5 M HCl, where alloyed steel remained without cracks over 300 h of exposure, whereas common 22MnB5 cracked in 12 h. A positive effect on HE resistance was also observed for the ε-carbides of SiMn and Ti, which may be formed by the auto-tempering effect of the steel during martensitic transformation or in the paint baking process [135]. The carbides reduced the content of diffusible hydrogen because they acted as irreversible hydrogen traps. Their formation was the best when performed at 200 °C, as higher temperatures led to a decrease in the UTS [156,160]. Atom probe tomography (APT) images showed that a higher amount of carbon found in ε-carbides corresponded to higher local concentrations of hydrogen [161].

Strain, which causes plastic deformation, results in a change in hydrogen flux and concentration in charged materials. Steel strained before hydrogen charging has a more defective structure with a higher concentration of dislocations, which increases its ability to trap hydrogen. Park et al. reported that plastically deformed steel delays the initial permeation of hydrogen but allows for a higher total hydrogen permeation current (see Figure 12) [162]. The delay of permeation current ramp-up is caused by a greater number of low-binding energy dislocations, which initially trap more hydrogen than a non-deformed material. After the traps become occupied by hydrogen, the permeation current of the deformed material increases above the limit of the non-deformed material because the occupied traps serve as effective diffusion pathways for hydrogen. The density of dislocations exponentially increases near the strain limit of 7%, as does the saturation concentration of absorbed hydrogen. This causes a higher susceptibility to cracking in more strained sheets. The lowest susceptibility to HE is detected between 1–3% of strain [163]. Strained areas also have less noble potential by up to 150 mV [164]. The potential difference between deformed and non-deformed areas changed in the presence of hydrogen. Hydrogen charging led to a

potential drop of an additional 300–500 mV. After removal from a charging cell, hydrogen started to escape, and the potential of the charged region grew [164].

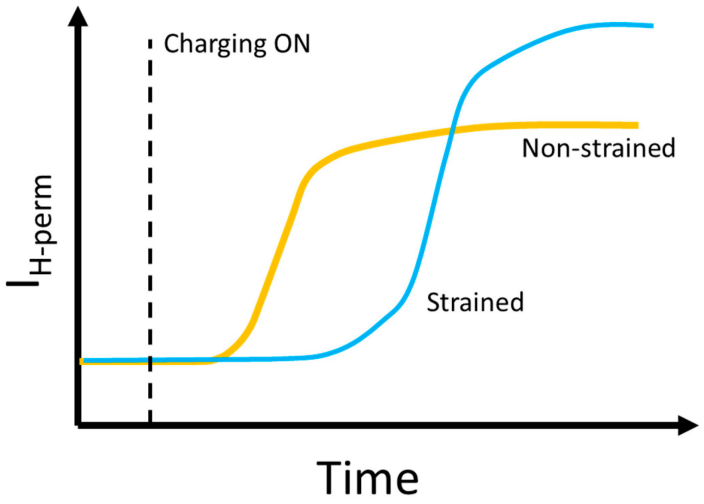

Figure 12. Schematics of change in the hydrogen permeation current of strained and non-strained material in the Devanathan–Stachurski experiment.

Since PHS panels are often painted, Lovicu et al. compared different martensitic steels in terms of their ability to trap hydrogen during coating application [30]. The hydrogen concentration in PHS increased up to 0.28 ppm. It was the highest for several investigated steel grades. The authors estimated that this amount of hydrogen should cause a loss of tensile strength lower than one percent. Compared to TRIP and cold-rolled steels, PHS showed a higher ability of hydrogen retention during the paint baking process at 180 °C. At room temperature, complete desorption of diffusible hydrogen from an uncoated steel sheet with a thickness of 1.5 mm should be achieved in 8 h [117].

Full recovery to original levels of mechanical properties is possible only for mildly charged steel. The process of paint baking can increase the ductility of a sample charged by a current density of 10 mA·cm^2 in 3 wt.% NaCl and 3 g·L^{-1} NH_4SCN for 48 h from 4 to 6%. In comparison with an uncharged sample, which showed 8% elongation, full recovery was not achieved, but the improvement of ductility provided by paint baking was 50% [156]. This indicates that a high concentration of diffusible hydrogen introduced by charging in harsh conditions induces irreversible damage through voids or blisters. This type of damage may be obtained by excessively aggressive electrochemical charging at 20 mA·cm^{-2} in 1 M H_2SO_4 [146]. At such conditions, hydrogen atoms in charged material may undergo recombination to molecules at lattice defects and cause blistering. Blisters originate from cracks present in the material (see Figure 13a). In PHS with a UTS close to 2000 MPa, cracks are formed under the surface. As a result of low ductility, cracks in the material connect, creating a crack propagating towards the surface (see Figure 13b). This effect is especially dangerous in welds of AHSS.

The effect of the parameters discussed above on HE is summarized in Table 4.

Table 4. Effect of selected parameters on the HE of PHS.

	Effect on PHS Behavior	References
UTS	Stronger is more susceptible to HE Depends on the steel (for 1800 MPa steel)	[17,147]
Hydrogen concentration	Limit diffusible hydrogen to 1.7 ppm Limit total hydrogen to 4 ppm Strength decreases up to 75% of the UTS at 8.5 ppm of total hydrogen	[29] [30]

Table 4. *Cont.*

	Effect on PHS Behavior	References
Austenitization	900 °C for 3–10 min to obtain the best HE resistance in fully martensitic structure results	[80,129,147,157]
Paint baking	180 °C for 10–30 min to remove diffusible hydrogen without decreasing the UTS	[29,62,156]
Prior austenitic grain size	Under 10 µm for the best mechanical properties; smaller PAGs are more prone to loss in ductility	[21,51,130]
Strain	Minimal influence at 1–3%; after charging, it may decrease corrosion resistance by influencing the OCP (less stable passive layer)	[163,164]
Precipitates	Nb precipitates increase HE resistance by lowering the diffusion coefficient and acting as irreversible traps ε-carbides (SiMn and Ti-based) form during paint baking and increase the HE resistance	[10,131,150,159,165]
Extreme charging conditions	More ductile PHS—cracks and blisters Less ductile PHS—microcracks forming large cracks Low H—ductile fracture with small dimples, necking	[146]
Fracture mechanism	Medium H—quasi-cleavage fractures along the (011) plane of martensitic laths High H—fracture initiated on the surface progressing with an intergranular facet mechanism, no necking	[20,147,159]

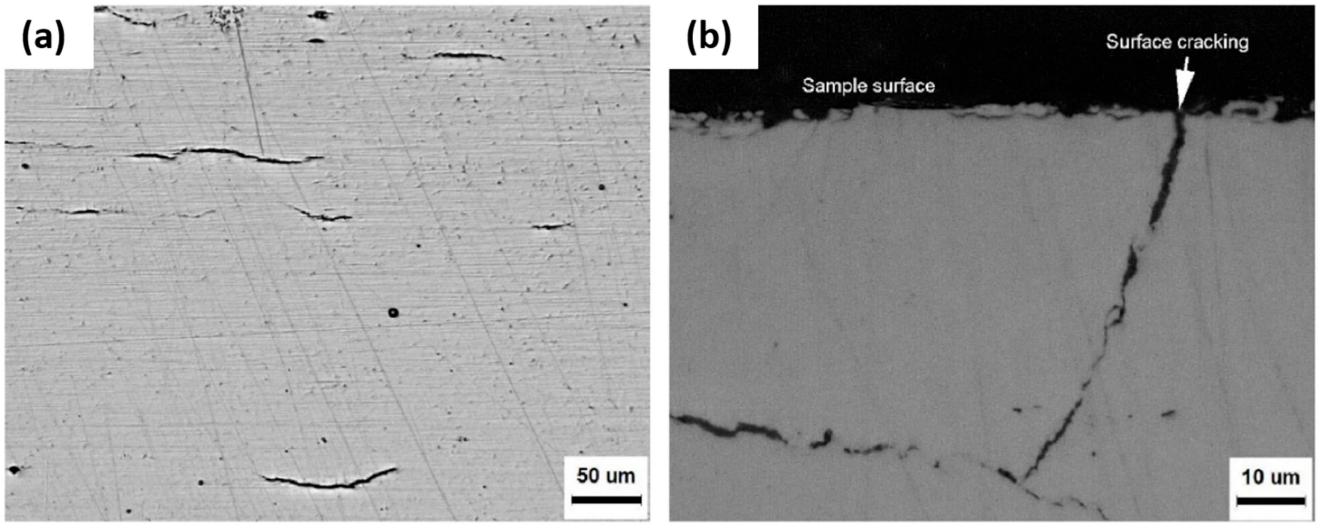

Figure 13. Cracking caused by excessive hydrogen charging: (**a**) smaller cracks under the surface and (**b**) the final crack propagating to the surface. Reprinted with permission from Ref. [146]. 2024, Elsevier.

6.2. Effect of Coating on HE of PHS

Diffusible hydrogen is first introduced into PHS GI during the austenitization step of hot stamping. This hydrogen is generated by hydrolysis of Zn with water vapor (Equation (15)). The liquid coating has a high diffusion coefficient, allowing for rapid hydrogen permeation. Initially, a layer of Fe_2Al_5 present at the interface between molten Zn and steel acts as a strong barrier hindering hydrogen transport through the interface to steel [166]. However, this layer is decomposed during the austenitization [77]. Still, the concentration of hydrogen in steel remains modest because of ZnO forming as a product of the hydrolysis reaction and protecting the zinc melt at the air–coating interface, which suppresses further absorption of hydrogen [77].

$$Zn(l) + H_2O(g) \rightarrow ZnO(s) + H_2(g) \quad (15)$$

Hydrogen absorbed during hot stamping is removed from the PHS GI during paint baking (Figure 7) at 180 °C or higher. Under such conditions, complete desorption of diffusible hydrogen occurs in less than 20 min [117]. At laboratory temperature, the desorption of hydrogen is slow from steel covered with a non-defective coating since the coating acts as a barrier. For a non-corroded, uncoated steel sheet with a thickness of 1.5 mm, it took 8 h to desorb diffusible hydrogen at laboratory temperature. Application of a PHS GI coating with a weight of 140 $g \cdot m^{-2}$ and austenitizing for 6 min increased the desorption time to 23 h [117].

In service, the coating effectively delays the introduction of hydrogen into steel. For a defect-free GI coating, the hydrogen diffusion coefficient is 2.3×10^{-10} $cm^2 \cdot s^{-1}$ [167]. However, if defects such as cracks penetrating the entire coating thickness are introduced, the efficient diffusion coefficient increases to 1.6×10^{-9} $cm^2 \cdot s^{-1}$ [162,167]. In the case of atmospheric exposure, hydrogen entry is realized through these defects due to galvanic coupling between the coating and steel at the defect area [168]. For PHS GI, cracks that form during the hot stamping process or by subsequent deformation of the material can serve as such defects [65,99]. There is a risk of deeper cracks caused by liquid metal embrittlement, which will result in uncovering the steel surface to a greater extent. While extensive cracking can be eliminated by optimizing austenitizing parameters, the formation of smaller through-coating cracks remains a problem for PHS GI [81,169]. Further cracks can form in the PHS GI coating under straining, primarily along grain boundaries, resulting in increased hydrogen absorption [162].

The hydrogen absorption rate caused by the galvanic coupling between the coating and steel may be affected by the presence of corrosion products. When corrosion products precipitate on the exposed steel substrate, the shift of open circuit potential (OCP) towards more noble values occurs, which reduces the cathodic overpotential. This decreases the galvanic couple activity and reduces the evolution rate of hydrogen on steel [162]. Corrosion products formed on the corroding coating also support a gradual decrease in the hydrogen entry [167]. During later stages of exposure to a corrosive environment, through-coating pits develop. Such new galvanic sites increase hydrogen absorption [99,162,167]. The time phase of enhanced hydrogen entry does not last very long for narrow defects because they become blocked by corrosion products [24,99].

The evolution of hydrogen absorption in GI coated steel was documented in wet/dry cycling in NaCl solution. As shown in Figure 14, hydrogen absorption reached a maximum in the 11th cycle. It is probable that defects penetrating the coating were introduced between cycles 5 and 11. As a result of the corrosion of the coating and opening of the steel surface, the potential of the galvanic couple shifted to more noble values, which may have decreased the rate of the HER. The H absorption may also have been hindered by corrosion product formation, which will block H entry [168]. This conclusion corresponds to Machackova et al. [99].

Under certain conditions, defects may be beneficial for suppressing HE [162]. If the material is pre-strained before exposure to a corrosive environment, narrow defects are introduced into the coating. When exposed to a corrosive environment with a sufficient supply of Cl^- ions, the coating dissolves more rapidly due to galvanic coupling, and the corrosion products quickly fill these defects. This quick process lowers the corrosion potential of the galvanic couple and reduces hydrogen entry. The strain field created in the steel by pre-straining traps hydrogen absorbed in the initial phase of exposure. If no additional hydrogen absorption occurred, a material strained by 4% performed better in a constant load test compared to a non-strained material. However, better performance heavily depends on the corrosive environment controlling the type of formed corrosion products [162,167].

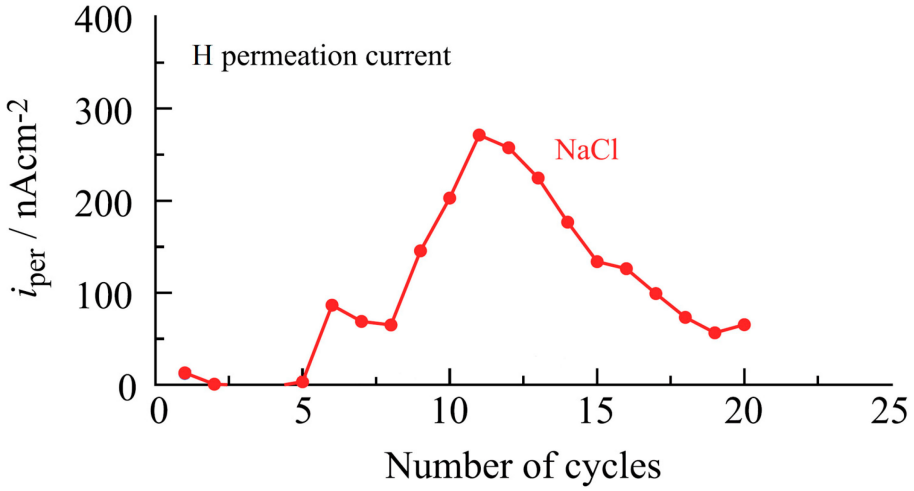

Figure 14. Change in hydrogen permeation current through GI coated steel subjected to a NaCl wet/dry cycling test. Reprinted from Ref. [168].

The importance of a corrosive environment was demonstrated by a comparison of defective and non-defective GI coating in 3.5 wt.% NaCl and 1 wt.% NH_4SCN solutions (Figure 15). Four-point bend samples exposed to the NaCl solution exhibited better performance due to the formation of corrosion products suppressing hydrogen entry in this environment [162].

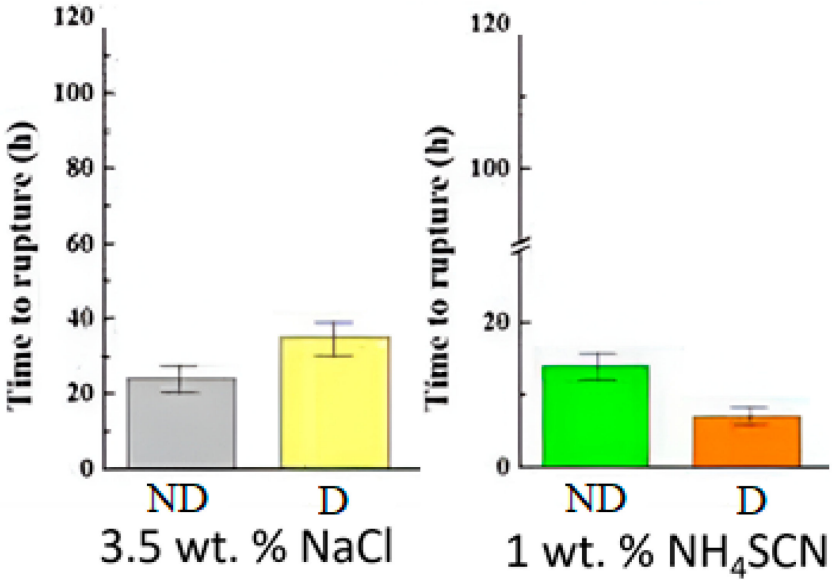

Figure 15. Comparison of four-point bend test rupture time of non-defective (ND) and defective (D) GI coated steel exposed in NaCl and NH_4SCN solutions. Reprinted with permission from Ref. [162]. 2024, Elsevier.

The influence of coatings on the fracture behavior of galvanized steel was investigated by Reumont et al. using the SSRT [27]. GI coated steel exhibited ductile fracture, whereas PHS GI exhibited transgranular fracture with striations perpendicular to the propagation direction of the crack, which is common for the HE of steel. The authors proposed that strained Zn–Fe phases exposed to 3 wt.% NaCl generate small cracks at their interface, which tend to open and propagate towards the steel surface. After reaching the surface of the steel, the coating facilitates hydrogen evolution on the steel, which creates conditions favorable for HE crack initiation.

Absorption of hydrogen into zinc coatings can result in a decrease in ductility and an increase in hardness. The results of Panagopoulos et al. suggest that hydrogen interaction with Zn can cause tension in the lattice by incorporating hydrogen and by possible formation of ZnH_2 hydrides [170]. The authors speculate that it might affect the formation of defects under strain and facilitate crack initiation in the steel.

The above-discussed effects are summarized in a schematic drawing in Figure 16.

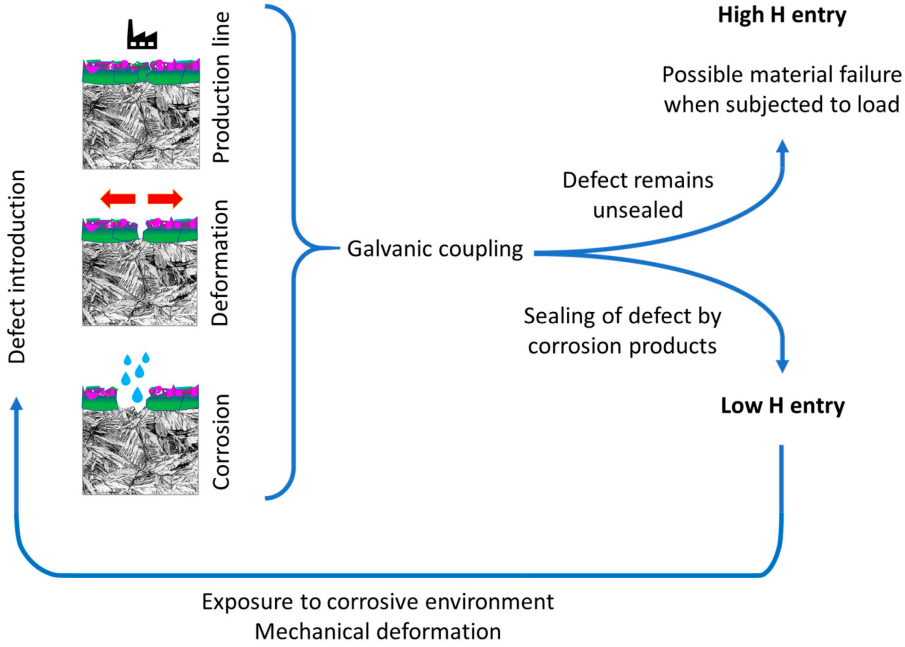

Figure 16. Schematics summarizing the influence of strain and corrosion processes on the HE of PHS GI.

7. Summary

Press-hardened steel has gained significance recently, mainly for its use in the automotive industry. PHS GI is affordable to manufacture and offers many advantages, including high strength and great corrosion resistance. The drawback of the material lies in its increased susceptibility to HE, which may result in a reduction in tensile strength and eventually even brittle fracture below the yield strength level. Hydrogen is first introduced into the material during manufacturing. It does not represent a major problem because hydrogen is removed by the paint baking process, and a car leaves the production factory hydrogen-free. Still, HE can be caused by corrosion-induced hydrogen.

The mechanical properties of bare PHS are given mainly by the steel grade and parameters of austenitization. The optimal setting of the austenitization process for the best tensile strength and toughness is at a temperature of 880–910 °C and a dwell time of 3–10 min depending on the material thickness [21,86,156]. It has been reported that the characteristics of the steel entering the austenitization step can significantly change the output properties, which indicates that tight control over the whole manufacturing process is necessary [47]. The susceptibility of PHS to HE is closely tied to the microstructure features of the steel, such as PAGs, martensitic laths, and carbides [33,51]. The impact of the size and morphology of both PAGs and martensitic laths on HE is confirmed. The resistance against HE decreases when the PAG size approaches 15 µm, and grains should ideally be elongated [51,130]. Based on the Hall–Petch strengthening law applied on a µm scale, finer PAGs should lead to higher strength. In contrast, structures with finer grains contain more grain boundaries, which can trap more hydrogen, resulting in a loss of ductility. A similar approach can be applied to finely dispersed martensitic laths, which are, thanks to high dislocation density and internal stress, more prone to HE [171]. Finely dispersed carbides of alloying elements such as Nb, V, Ti, and Mo can be used to suppress HE because

they irreversibly trap and immobilize hydrogen [150,161]. The precipitate density can be adjusted by conditions of austenitization and paint baking [156].

Considering parameters such as toughness, ductility in an austenitized and quenched state, corrosion resistance, hydrogen retention, and hydrogen charging via corrosion reactions, PHS GI offers a good combination of benefits [77]. The ideal conditions for the formation of the PHS GI coating are similar to the conditions necessary for full austenitization of the steel without PAG coarsening. It is advised to set the parameters of austenitization in such a way as to obtain 10 vol.% of Γ-ZnFe. The Γ-ZnFe phase in galvanic coupling with α-Fe(Zn) corrodes preferentially and offers further protection to steel during atmospheric corrosion [25]. The dwell time of austenitization also affects the distribution of the decomposed Fe_2Al_5 layer and the consequent diffusion of hydrogen through the coating [145].

Compared to GI coatings, PHS GI has superior corrosion resistance. Due to a more positive free corrosion potential, it can be expected to cause a lower polarization of steel and thus a lower tendency to form hydrogen in defects [25,70]. Although it contains cracks that allow for rapid contact between steel and a corrosive environment and hydrogen entry, it has been reported that they become blocked by corrosion products, which suppress further absorption of hydrogen [167]. The formation of corrosion products able to suppress HE depends on exposure conditions [162]. Permanent straining can be risky due to repeated formation of fresh defects in the brittle coating [24,27].

8. Direction of Future Research

To improve the resistance of PHS GI against HE, changing the structure of the steel can be one of the approaches. For steel with a fully martensitic structure, the HE resistance can be enhanced through microstructural refinement and the formation of carbides.

Refinement of the PAG size is essential for increasing the strength and ductility of PHS. The UTS of steel containing hydrogen was reported to remain unchanged in a grain size ranging from 15 to 40 μm [51,130]. Steels with PAG sizes finer than 15 μm tend to exhibit an increased HE susceptibility at a higher H concentration in the structure. The problem of controlling the PAG size is further complicated by possible local microstructure changes induced by deformation during hot stamping. Considering only the PAG size, it is agreed that it should be larger than 15 μm or higher hydrogen concentrations must be avoided.

To further enhance the strength, two critical aspects must be addressed: grain size reduction and the control of diffusible hydrogen. Both of these challenges can be mitigated by adding Nb, Ti, and V, which form carbides that inhibit grain coarsening during austenitization [33,150,159]. These carbides can trap diffusible hydrogen, potentially reducing its concentration to levels where steels with PAG sizes below 15 μm are less susceptible to HE. Finding the balance between the composition and austenitization parameters, which will deliver HE-resistant steel with high strength, is the subject of further investigation [109].

The other approach to mitigating HE is the introduction of another phase less prone to cracking than martensite. An increasing volume of RA provides better resistance against HE, and it can be achieved by alloying with Al [172]. The volume and the morphology of austenite play a significant role in suppressing HE, with thick filmy RA being more efficient than blocky RA [173]. Ways of incorporating such structures into PHS, their formation, and the effect on HE are still largely unknown.

The effect of a PHS GI coating on the absorption of hydrogen and its transport into steel is also not fully understood. Although absorption of hydrogen takes place mainly in defects present in the coating, it can be expected that corrosion reactions on the surface cause additional hydrogen entry into the coating. The rate of the HER is affected by the mutual galvanic effect of phases present in the PHS GI [162]. Hydrogen concentrations and diffusion rates in the phases are not known. The possibility of the coating serving as a reservoir of hydrogen entering the steel substrate has not been refuted. The barrier effect of the Fe_2Al_5 layer has also not been completely described yet [77,117]. For PHS AS, it has been shown that hydrogen is trapped mostly in the dislocation strain fields of steel, and the

amount of H trapped in the thin coating layer is negligible [152]. Models of single-phase structures or single-phase coatings need to be studied to answer these questions.

The types of corrosion products forming on GI coated steel and PHS GI have been described; however, there is not much knowledge on the effect of particular corrosion products on hydrogen formation, absorption, and desorption [9,174]. Is there a way to set favorable conditions promoting the formation of more protective corrosion products? Research should focus on the stability and protectiveness of corrosion products, especially in terms of their long-term ability to seal defects under different exposure conditions. For instance, alloying PHS GI coating with elements such as Al or Mg can help to increase the atio of stable corrosion products that efficiently block coating defects [175,176].

9. Conclusions

- The tensile strength of PHS depends on the composition, PAG size, presence of carbides, and processing parameters of the PHS. All those factors also influence the susceptibility to HE.
- The optimal parameters of austenitization for bare PHS and PHS GI are 880–910 °C at a dwell time of 3–10 min. Heat treatment at 120–200 °C for 10–30 min after austenitization is mandatory to release the hydrogen absorbed during the hot stamping process.
- Nb, Ti, and V carbides can suppress the susceptibility of PHS to HE.
- For PHS with a UTS of 1800 MPa, the most significant drop in the UTS was observed from 4 ppm of total hydrogen, which corresponded to 1.7 ppm of diffusible hydrogen.
- Compared to the GI coated steel, PHS GI offers increased corrosion protection. The PHS GI coating is thicker, harder, and more brittle.
- In coating defects, steel is cathodically protected by the coating when exposed to a corrosive environment.
- Hydrogen evolution caused by galvanic coupling is hindered by corrosion products, which can seal the defects. This effect is important mainly for narrow defects and depends on the corrosion environment.

Author Contributions: Conceptualization, T.K., T.P., T.S. and R.S.; methodology, T.P., N.M. and R.S.; investigation, T.K. and N.M.; writing—original draft preparation, T.K. and N.M.; writing—review and editing, N.M., T.P., T.S. and R.S. All authors have read and agreed to the published version of the manuscript.

Funding: This research was supported by the grant of University of Chemistry and Technology, Prague; Specific university research—grant No. A2_FCHT_2024_082.

Data Availability Statement: The data presented in this study are available on request from the corresponding author. The data are not publicly available due to privacy restrictions.

Acknowledgments: voestalpine Stahl GmbH is thanked for providing financial and material support.

Conflicts of Interest: Authors Thomas Steck and Reza Sharif were employed by the company voestalpine Stahl GmbH. The remaining authors declare that the research was conducted in the absence of any commercial or financial relationships that could be construed as a potential conflict of interest.

References

1. Lesch, C.; Kwiaton, N.; Klose, F.B. Advanced high strength steels (AHSS) for automotive applications− tailored properties by smart microstructural adjustments. *Steel Res. Int.* **2017**, *88*, 1700210. [CrossRef]
2. Pan, Y.; Xiong, Y.; Wu, L.; Diao, K.; Guo, W. Lightweight design of an automotive battery-pack enclosure via advanced high-strength steels and size optimization. *Int. J. Automot. Technol.* **2021**, *22*, 1279–1290. [CrossRef]
3. Taylor, T.; Fourlaris, G.; Clough, A. Effect of carbon and microalloy additions on hot-stamped boron steel. *Mater. Sci. Technol.* **2017**, *33*, 1964–1977. [CrossRef]
4. Billur, E. Hot stamping of ultra high-strength steels. In *From a Technological and Business Perspective*; Springer: Cham, Switzerland, 2019.

5. Múnera, D.D.; Pic, A.; Abou-Khalil, D.; Shmit, F.; Pinard, F. Innovative press hardened steel based laser welded blanks solutions for weight savings and crash safety improvements. *SAE Int. J. Mater. Manuf.* **2009**, *1*, 472–479. [CrossRef]
6. Tisza, M.; Czinege, I. Comparative study of the application of steels and aluminium in lightweight production of automotive parts. *Int. J. Lightweight Mater. Manuf.* **2018**, *1*, 229–238. [CrossRef]
7. Cherubini, A.; Bacchi, L.; Corsinovi, S.; Beghini, M.; Valentini, R. Hydrogen Embrittlement in Advanced High Strength Steels and Ultra High Strength Steels: A new investigation approach. *Procedia Struct. Integr.* **2018**, *13*, 753–762. [CrossRef]
8. Miller, W.; Zhuang, L.; Bottema, J.; Wittebrood, A.J.; De Smet, P.; Haszler, A.; Vieregge, A. Recent development in aluminium alloys for the automotive industry. *Mater. Sci. Eng. A* **2000**, *280*, 37–49. [CrossRef]
9. Autengruber, R.; Luckeneder, G.; Hassel, A.W. Corrosion of press-hardened galvanized steel. *Corros. Sci.* **2012**, *63*, 12–19. [CrossRef]
10. Cao, Z.; Wang, Z.; Ngiam, Y.; Luo, Z.; Geng, Z.; Wang, J.; Zhang, Y.; Huang, M. Hydrogen Embrittlement Evaluation and Prediction in Press-Hardened Steels. *Steel Res. Int.* **2023**, *94*, 2200685. [CrossRef]
11. Funakawa, Y.; Nagataki, Y. High strength steel sheets for weight reduction of automotives. *JFE Tech. Rep.* **2019**, *24*, 1–5.
12. Shi, T.; Zhao, F.; Hao, H.; Liu, Z. *Costs, Benefits and Range: Application of Lightweight Technology in Electric Vehicles*; SAE Technical Paper; SAE International: Warrendale, PA, USA, 2019.
13. Diniz, F.; Morais, C.; Luiz, A.; Simplício, A.; Lima, L.; Silvério, R. *Emergent Market Dealers Serviceability Challenges in Vehicles with PHS Structure*; SAE Technical Paper; SAE International: Warrendale, PA, USA, 2016.
14. Chen, X.; Wang, X.; Sun, Q.; Hu, Z.; Huan, P.; Yi, G.; Hiromi, N.; Di, H.; Sun, L. Improving the mechanical properties of PHS laser welded joints by adding Ni foil to suppress δ-ferrite. *J. Mater. Res. Technol.* **2020**, *9*, 5184–5193. [CrossRef]
15. Zhang, Z.; Wang, X.; Sun, Q.; Yang, B.; Xiong, L.; Liu, H. Study on microstructure and properties of laser dissimilar welded joints of ultra-high strength PHS1500/PHS2000 steel. *Opt. Laser Technol.* **2022**, *150*, 107933. [CrossRef]
16. Su, J.; Qiu, X.; Xing, F.; Luo, C.; Ruan, Y. Transformation of microstructure and properties of heterogeneous PHS laser welded joint of unequal thickness before and after hot forming. *Mater. Lett.* **2022**, *306*, 130918. [CrossRef]
17. Valentini, R.; Tedesco, M.M.; Corsinovi, S.; Bacchi, L.; Villa, M. Investigation of mechanical tests for hydrogen embrittlement in automotive PHS steels. *Metals* **2019**, *9*, 934. [CrossRef]
18. Krauss, G. Martensite in steel: Strength and structure. *Mater. Sci. Eng. A* **1999**, *273*, 40–57. [CrossRef]
19. Turetta, A.; Bruschi, S.; Ghiotti, A. Investigation of 22MnB5 formability in hot stamping operations. *J. Mater. Process. Technol.* **2006**, *177*, 396–400. [CrossRef]
20. Chai, Z.; Lu, Q.; Hu, J.; Wang, L.; Wang, Z.; Wang, J.; Xu, W. Effect of retained austenite on the fracture behavior of a novel press-hardened steel. *J. Mater. Sci. Technol.* **2023**, *135*, 34–45. [CrossRef]
21. Cho, L.; Bradley, P.; Lauria, D.; Connolly, M.; Seo, E.; Findley, K.; Speer, J.; Golem, L.; Slifka, A. Effects of hydrogen pressure and prior austenite grain size on the hydrogen embrittlement characteristics of a press-hardened martensitic steel. *Int. J. Hydrogen Energy* **2021**, *46*, 24425–24439. [CrossRef]
22. Kurz, T.; Luckeneder, G.; Manzenreiter, T.; Schwinghammer, H.; Sommer, A. *Zinc Coated Press-Hardening Steel-Challenges and Solutions*; SAE Technical Paper; SAE International: Warrendale, PA, USA, 2015.
23. Wan, X.; Zhao, Y.; Li, Y.; Zhou, J. The Application of Press Hardened Steel on Volvo XC90 Gen II. In *Advanced High Strength Steel and Press Hardening: Proceedings of the 2nd International Conference (ICHSU2015), Changsha, China, 15–18 October 2016*; World Scientific: Singapore, 2016; pp. 669–674.
24. Drillet, P. Overview on Coatings Developed on Press Hardened Steels for Automotive Applications. In *Advanced High Strength Steel and Press Hardening: Proceedings of the 4th International Conference on Advanced High Strength Steel and Press Hardening (ICHSU2018), Hefei, China, 20–22 August 2018*; World Scientific: Singapore, 2019; p. 55.
25. Dever, C.; Kish, J.; McDermid, J. Corrosion Properties of Hot Dip Zinc Galvanized Coatings on 22MnB5 Press Hardened Steels. In Proceedings of the GALVATECH 2017: 11th International Conference on Zinc and Zinc Alloy Coated Steel Sheet, Tokyo, Japan, 12–16 November 2017.
26. Dosdat, L.; Petitjean, J.; Vietoris, T.; Clauzeau, O. Corrosion resistance of different metallic coatings on press-hardened steels for automotive. *Steel Res. Int.* **2011**, *82*, 726–733. [CrossRef]
27. Reumont, G.; Vogt, J.; Iost, A.; Foct, J. The effects of an Fe–Zn intermetallic-containing coating on the stress corrosion cracking behavior of a hot-dip galvanized steel. *Surf. Coat. Technol.* **2001**, *139*, 265–271. [CrossRef]
28. Rudomilova, D.; Prošek, T.; Ström, M. Hydrogen entry into steel under corrosion products. *Corrosion* **2021**, *77*, 427–432. [CrossRef] [PubMed]
29. Lee, S.-J.; Ronevich, J.A.; Krauss, G.; Matlock, D.K. Hydrogen embrittlement of hardened low-carbon sheet steel. *ISIJ Int.* **2010**, *50*, 294–301. [CrossRef]
30. Lovicu, G.; Bottazzi, M.; D'aiuto, F.; De Sanctis, M.; Dimatteo, A.; Santus, C.; Valentini, R. Hydrogen embrittlement of automotive advanced high-strength steels. *Metall. Mater. Trans. A* **2012**, *43*, 4075–4087. [CrossRef]
31. Cottis, R.A. *Hydrogen Embrittlement*; Elsevier: Manchester, UK, 2010; pp. 903–921.
32. Jian, B.; Wang, L.; Mohrbacher, H.; Lu, H.Z.; Wang, W.J. Development of niobium alloyed press hardening steel with improved properties for crash performance. *Adv. Mater. Res.* **2015**, *1063*, 7–20. [CrossRef]
33. Lin, L.; Li, B.-S.; Zhu, G.-M.; Kang, Y.-L.; Liu, R.-D. Effect of niobium precipitation behavior on microstructure and hydrogen induced cracking of press hardening steel 22MnB5. *Mater. Sci. Eng. A* **2018**, *721*, 38–46. [CrossRef]

34. Järvinen, H.; Honkanen, M.; Patnamsetty, M.; Järn, S.; Heinonen, E.; Jiang, H.; Peura, P. Press hardening of zinc-coated boron steels: Role of steel composition in the development of phase structures within coating and interface regions. *Surf. Coat. Technol.* **2018**, *352*, 378–391. [CrossRef]
35. Hannula, J.; Porter, D.A.; Kaijalainen, A.; Kömi, J. Evaluation of Mechanical Properties and Microstructures of Molybdenum and Niobium Microalloyed Thermomechanically Rolled High-Strength Press Hardening Steel. *JOM* **2019**, *71*, 2405–2412. [CrossRef]
36. Thakkar, R. *Correlation between Microstructure and Mechanical Properties of Press-Hardenable Steels for Various Quenching Rates*; University of Windsor: Windsor, ON, Canada, 2022.
37. Järvinen, H.; Honkanen, M.; Järvenpää, M.; Peura, P. Effect of paint baking treatment on the properties of press hardened boron steels. *J. Mater. Process. Technol.* **2018**, *252*, 90–104. [CrossRef]
38. Järvinen, H. Processing and Properties of Hot-Dip Galvanized Press-Hardening Steels. Ph.D. Thesis, Tampere University, Tampere, Finland, 2021. Available online: https://trepo.tuni.fi/handle/10024/134628 (accessed on 27 January 2024).
39. Zhao, Y.; Yang, D.; Qin, Z.; Chu, X.; Liu, J.; Zhao, Z. A novel hot stamping steel with superior mechanical properties and antioxidant properties. *J. Mater. Res. Technol.* **2022**, *21*, 1944–1959. [CrossRef]
40. Thelning, K.-E. *Steel and Its Heat Treatment*; Butterworth-Heinemann: Oxford, UK, 2013.
41. Åkerström, P.; Oldenburg, M. Austenite decomposition during press hardening of a boron steel—Computer simulation and test. *J. Mater. Process. Technol.* **2006**, *174*, 399–406. [CrossRef]
42. Tungtrongpairoj, J.; Uthaisangsuk, V.; Bleck, W. Determination of yield behaviour of boron alloy steel at high temperature. *J. Met. Mater. Miner.* **2009**, *19*, 29–38.
43. Roy, S.; Karmakar, A.; Mukherjee, S.; Kundu, S.; Srivastava, D.; Chakrabarti, D. Effect of starting microstructure on austenite grain sizes developed after reheating of HSLA steel. *Mater. Sci. Technol.* **2014**, *30*, 1142–1153. [CrossRef]
44. voestalpine AG. Uncoated Hot-Forming Steels for the Production of Press-Hardened Components. Available online: https://www.voestalpine.com/ultralights/en/content/download/26088/file/DB_phs_uncoated_E_151118.pdf (accessed on 4 August 2024).
45. Kondratiuk, J.; Kuhn, P.; Labrenz, E.; Bischoff, C. Zinc coatings for hot sheet metal forming: Comparison of phase evolution and microstructure during heat treatment. *Surf. Coat. Technol.* **2011**, *205*, 4141–4153. [CrossRef]
46. Zhou, J.; Wang, B.-Y.; Huang, M.-D.; Cui, D. Effect of hot stamping parameters on the mechanical properties and microstructure of cold-rolled 22MnB5 steel strips. *Int. J. Miner. Metall. Mater.* **2014**, *21*, 544–555. [CrossRef]
47. Järvinen, H.; Isakov, M.; Nyyssönen, T.; Järvenpää, M.; Peura, P. The effect of initial microstructure on the final properties of press hardened 22MnB5 steels. *Mater. Sci. Eng. A* **2016**, *676*, 109–120. [CrossRef]
48. Golem, L.; Cho, L.; Speer, J.G.; Findley, K.O. Influence of austenitizing parameters on microstructure and mechanical properties of Al-Si coated press hardened steel. *Mater. Des.* **2019**, *172*, 107707. [CrossRef]
49. He, L.F.; Zhao, G. Research on Mechanical Properties of 22MnB5 Steel Quenched in a Steel Die. *J. Shanghai Jiaotong Univ.* **2011**, *16*, 129–132. [CrossRef]
50. Barcellona, A.; Palmeri, D. Effect of plastic hot deformation on the hardness and continuous cooling transformations of 22MnB5 microalloyed boron steel. *Metall. Mater. Trans. A* **2009**, *40*, 1160–1174. [CrossRef]
51. Liu, Y.; Lian, J.; Han, X.; Yang, Y.; Yuan, H. Hydrogen embrittlement studies of hot-stamped boron steel with different prior austenite grain sizes. *J. Mater. Sci.* **2023**, *58*, 18187–18206. [CrossRef]
52. Chai, Z.; Wang, L.; Wang, Z.; Lu, Q.; Hu, J.; Sun, W.; Wang, J.; Xu, W. Cr-enriched carbide induced stabilization of austenite to improve the ductility of a 1.7 GPa− press-hardened steel. *Scr. Mater.* **2023**, *224*, 115108. [CrossRef]
53. Wei, X.; Chai, Z.; Lu, Q.; Hu, J.; Liu, Z.; Lai, Q.; Wang, J.; Xu, W. Cr-alloyed novel press-hardening steel with superior combination of strength and ductility. *Mater. Sci. Eng. A* **2021**, *819*, 141461. [CrossRef]
54. Abbasi, M.; Naderi, M.; Saeed-Akbari, A. Isothermal versus non-isothermal hot compression process: A comparative study on phase transformations and structure–property relationships. *Mater. Des.* **2013**, *45*, 1–5. [CrossRef]
55. Hutchinson, B.; Hagström, J.; Karlsson, O.; Lindell, D.; Tornberg, M.; Lindberg, F.; Thuvander, M. Microstructures and hardness of as-quenched martensites (0.1–0.5% C). *Acta Mater.* **2011**, *59*, 5845–5858. [CrossRef]
56. Lee, J.A.; Woods, S. Hydrogen Embrittlement. 2016. Available online: https://ntrs.nasa.gov/citations/20160005654 (accessed on 15 March 2024).
57. Khan, M.S.; Razmpoosh, M.; Biro, E.; Zhou, Y. A review on the laser welding of coated 22MnB5 press-hardened steel and its impact on the production of tailor-welded blanks. *Sci. Technol. Weld. Join.* **2020**, *25*, 447–467. [CrossRef]
58. Betiku, O.T.; Shojaee, M.; Sherepenko, O.; Midawi, A.R.; Chertov, A.M.; Ghassemi-Armaki, H.; Maev, R.G.; Biro, E. Optimizing post-weld performance of press-hardened steel resistance spot welds by controlling fusion zone porosity. *Weld. World* **2022**, *66*, 1733–1746. [CrossRef]
59. Akafuah, N.K.; Poozesh, S.; Salaimeh, A.; Patrick, G.; Lawler, K.; Saito, K. Evolution of the automotive body coating process—A review. *Coatings* **2016**, *6*, 24. [CrossRef]
60. Venezuela, J.; Lim, F.Y.; Liu, L.; James, S.; Zhou, Q.; Knibbe, R.; Zhang, M.; Li, H.; Dong, F.; Dargusch, M.S. Hydrogen embrittlement of an automotive 1700 MPa martensitic advanced high-strength steel. *Corros. Sci.* **2020**, *171*, 108726. [CrossRef]
61. Hilditch, T.; Lee, S.; Speer, J.; Matlock, D. *Response to Hydrogen Charging in High Strength Automotive Sheet Steel Products*; SAE Technical Paper; SAE International: Warrendale, PA, USA, 2003; ISSN 0148-7191.
62. Ding, C.; Zhao, H.; Xu, D.; Liu, Z.; Deng, C.; Hu, B.; Song, W.; Wang, Y.; Luo, H. Revisit of bake hardening mechanism: Influence of baking on tensile properties of press hardening steels. *Mater. Sci. Eng. A* **2024**, *896*, 146276. [CrossRef]

63. Zou, S. *Understanding the Influence of Paint Baking on the HE Susceptibility of Some AHSS*; The University of Queensland: Saint Lucia, Australia, 2018.
64. Panossian, Z.; Mariaca, L.; Morcillo, M.; Flores, S.; Rocha, J.; Peña, J.; Herrera, F.; Corvo, F.; Sanchez, M.; Rincon, O. Steel cathodic protection afforded by zinc, aluminium and zinc/aluminium alloy coatings in the atmosphere. *Surf. Coat. Technol.* **2005**, *190*, 244–248. [CrossRef]
65. Chen, L.; Chen, W.; Cao, M.; Li, X. Performance Comparison of Zn-Based and Al–Si Based Coating on Boron Steel in Hot Stamping. *Materials* **2021**, *14*, 7043. [CrossRef]
66. Ahner, C.; Maaß, P.; Peißker, P. *Handbook of Hot-Dip Galvanization*; John Wiley & Sons: New York, NY, USA, 2011.
67. da Costa Ximenes, D.A.; Moreira, L.P.; de Carvalho, J.E.R.; Leite, D.N.F.; Toledo, R.G.; da Silva Dias, F.M. Phase transformation temperatures and Fe enrichment of a 22MnB5 Zn-Fe coated steel under hot stamping conditions. *J. Mater. Res. Technol.* **2020**, *9*, 629–635. [CrossRef]
68. Ghanbari, Z.N.; Speer, J.G.; Findley, K.O. Coating Evolution and Mechanical Behavior of Zn-Coated Press-Hardening Sheet Steel. In Proceedings of the 5th International Conference on Hot Sheet Metal Forming of High-Performance Steel, Toronto, ON, Canada, 31 May–3 June 2015.
69. Peng, H.; Peng, W.; Lu, R.; Wu, G.; Zhang, J. Diffusion and cracking behavior involved in hot press forming of Zn coated 22MnB5. *J. Alloys Compd.* **2019**, *806*, 195–205. [CrossRef]
70. Fan, D.W.; De Cooman, B.C. State-of-the-knowledge on coating systems for hot stamped parts. *Steel Res. Int.* **2012**, *83*, 412–433. [CrossRef]
71. Eleuterio, H.; Barbosa, A.; Buono, V. Optimization of Heat Treatment During Hot Stamping of PHS1500 Steel with Galvannealed Coating. In Proceedings of the International Symposium on New Developments in Advanced High-Strength Sheet Steels, Vail, CO, USA, 19–22 June 2023.
72. Wienströer, S.; Fransen, M.; Mittelstädt, H.; Nazikkol, C.; Völker, M. Zinc/Iron phase transformation studies on galvannealed steel coatings by X-ray diffraction. *ICDD* **2003**, *46*, 291–296.
73. Autengruber, R.; Luckeneder, G.; Kolnberger, S.; Faderl, J.; Hassel, A.W. Surface and coating analysis of press-hardened hot-dip galvanized steel sheet. *Steel Res. Int.* **2012**, *83*, 1005–1011. [CrossRef]
74. Marder, A. The metallurgy of zinc-coated steel. *Prog. Mater Sci.* **2000**, *45*, 191–271. [CrossRef]
75. Shi, Z.-Z.; Gao, X.-X.; Chen, H.-T.; Liu, X.-F.; Li, A.; Zhang, H.-J.; Wang, L.-N. Enhancement in mechanical and corrosion resistance properties of a biodegradable Zn-Fe alloy through second phase refinement. *Mater. Sci. Eng. C* **2020**, *116*, 111197. [CrossRef]
76. Xhoffer, C.; Dillen, H.; Cooman, B.D.; Hubin, A. Quantitative phase analysis of galvannealed coatings by coulometric stripping. *J. Appl. Electrochem.* **1999**, *29*, 209–219. [CrossRef]
77. Jo, K.R.; Cho, L.; Sulistiyo, D.H.; Seo, E.J.; Kim, S.W.; De Cooman, B.C. Effects of Al-Si coating and Zn coating on the hydrogen uptake and embrittlement of ultra-high strength press-hardened steel. *Surf. Coat. Technol.* **2019**, *374*, 1108–1119. [CrossRef]
78. Belin, C.H.; Belin, R.C. Synthesis and crystal structure determinations in the Γ and δ phase domains of the iron–zinc system: Electronic and bonding analysis of $Fe_{13}Zn_{39}$ and $FeZn_{10}$, a subtle deviation from the Hume–Rothery standard? *J. Solid State Chem.* **2000**, *151*, 85–95. [CrossRef]
79. Murugan, S.P.; Kim, J.; Kim, J.; Wan, Y.; Lee, C.; Jeon, J.B.; Park, Y.-D. Role of liquid Zn and α-Fe (Zn) on liquid metal embrittlement of medium Mn steel: An ex-situ microstructural analysis of galvannealed coating during high temperature tensile test. *Surf. Coat. Technol.* **2020**, *398*, 126069. [CrossRef]
80. Li, X.; Ma, W.; Zheng, X.; Shao, R.; Zhang, Y. Effect of Heat Treatment on the Formability of Zn-Coated Hot Stamping Steel. *Steel Res. Int.* **2022**, *93*, 2100725. [CrossRef]
81. Lee, C.W.; Fan, D.W.; Sohn, I.R.; Lee, S.-J.; De Cooman, B.C. Liquid-metal-induced embrittlement of Zn-coated hot stamping steel. *Metall. Mater. Trans. A* **2012**, *43*, 5122–5127. [CrossRef]
82. Lee, C.W.; Choi, W.S.; Cho, Y.R.; De Cooman, B.C. Surface oxide formation during rapid heating of Zn-coated press hardening steel. *ISIJ Int.* **2014**, *54*, 2364–2368. [CrossRef]
83. Gaderbauer, W.; Arndt, M.; Truglas, T.; Steck, T.; Klingner, N.; Stifter, D.; Faderl, J.; Groiss, H. Effects of alloying elements on surface oxides of hot–dip galvanized press hardened steel. *Surf. Coat. Technol.* **2020**, *404*, 126466. [CrossRef]
84. Wang, K.; Zhu, B.; Wang, Z.; Liu, Y.; Wang, L.; Zhang, Y.; Li, S. Successive phase and morphology evolution of galvannealed coating in hot stamping and diffusion modeling of α-Fe (Zn)/steel system considering the effect of Zn concentration. *Surf. Coat. Technol.* **2019**, *380*, 125036. [CrossRef]
85. Bhattacharya, D.; Cho, L.; Marshall, D.; Walker, M.; Van Der Aa, E.; Pichler, A.; Ghassemi-Armaki, H.; Findley, K.; Speer, J. Liquid metal embrittlement susceptibility of two Zn-Coated advanced high strength steels of similar strengths. *Mater. Sci. Eng. A* **2021**, *823*, 141569. [CrossRef]
86. Goodwin, F.; Silva, E. North American Zinc-based Sheet Steel Coatings Technology and Production: Status and Opportunities. In Proceedings of the 9th International Conference on Zinc and Zinc Alloy Coated Steel Sheet, Beijing, China, 1 September 2013.
87. Drillet, P.; Grigorieva, R.; Leuillier, G.; Vietoris, T. Study of Cracks Propagation Inside the Steel on Press Hardened Steel Zinc Based Coatings. La Metallurgia Italiana. Available online: https://www.aimnet.it/allpdf/pdf_pubbli/gen12/DRILLET.pdf (accessed on 3 November 2024).

88. Hayashida, T.M.S.; Takebayashi, H. Zinc-Oxide Formation on Zinc-Coated Steel Sheet During Hot Stamping. In Proceedings of the 13th International Conference on Zinc & Zinc Alloy Coated Steel Sheet (GALVATECH 2023), COEX, Seoul, Republic of Korea, 15–19 October 2023.
89. Mason, B. Mineralogical aspects of the system FeO–Fc_2O_3–MnO–Mn_2O_3. *GFF* **1943**, *65*, 97–180. [CrossRef]
90. Gerberich, W.; Stauffer, D.; Sofronis, P. A coexistent view of hydrogen effects on mechanical behavior of crystals: HELP and HEDE. In Proceedings of the 2008 International Hydrogen Conference—Effects of Hydrogen on Materials, Jackson, WY, USA, 7–10 September 2009; pp. 38–45.
91. Li, X.; Ma, X.; Zhang, J.; Akiyama, E.; Wang, Y.; Song, X. Review of hydrogen embrittlement in metals: Hydrogen diffusion, hydrogen characterization, hydrogen embrittlement mechanism and prevention. *Acta Metall. Sin.* **2020**, *33*, 759–773. [CrossRef]
92. Wang, Z.; Lu, Q.; Cao, Z.; Chen, H.; Huang, M.; Wang, J. Review on hydrogen embrittlement of press-hardened steels for automotive applications. *Acta Metall. Sin.* **2023**, *36*, 1123–1143. [CrossRef]
93. Kim, H.-J.; Jung, H.-Y.; Jung, S.-P.; Son, J.-H.; Hyun, J.-S.; Kim, J.-S. Hydrogen Absorption and Desorption Behavior on Aluminum-Coated Hot-Stamped Boron Steel during Hot Press Forming and Automotive Manufacturing Processes. *Materials* **2021**, *14*, 6730. [CrossRef] [PubMed]
94. Schwedler, O.; Zinke, M.; Jüttner, S. Determination of hydrogen input in welded joints of press-hardened 22MnB5 steel. *Weld. World* **2014**, *58*, 339–346. [CrossRef]
95. Aiello, F.; Beghini, M.; Belardini, C.M.; Bertini, L.; Macoretta, G.; Monelli, B.D.; Valentini, R. Proposal of a hydrogen embrittlement index for a martensitic advanced high-strength steel. *Corros. Sci.* **2023**, *222*, 111357. [CrossRef]
96. Cho, L.; Sulistiyo, D.H.; Seo, E.J.; Jo, K.R.; Kim, S.W.; Oh, J.K.; Cho, Y.R.; De Cooman, B.C. Hydrogen absorption and embrittlement of ultra-high strength aluminized press hardening steel. *Mater. Sci. Eng. A* **2018**, *734*, 416–426. [CrossRef]
97. Kim, H.-J.; Park, H.-K.; Lee, C.-W.; Yoo, B.-G.; Jung, H.-Y. Baking effect on desorption of diffusible hydrogen and hydrogen embrittlement on hot-stamped boron martensitic steel. *Metals* **2019**, *9*, 636. [CrossRef]
98. Chida, T.; Hagihara, Y.; Akiyama, E.; Iwanaga, K.; Takagi, S.; Hayakawa, M.; Ohishi, H.; Hirakami, D.; Tarui, T. Comparison of constant load, SSRT and CSRT methods for hydrogen embrittlement evaluation using round bar specimens of high strength steels. *ISIJ Int.* **2016**, *56*, 1268–1275. [CrossRef]
99. Macháčková, N.; Rudomilova, D.; Prošek, T. Respirometry, a new approach for investigation of the relationship between corrosion-induced hydrogen evolution and its entry into metallic materials. *Int. J. Hydrogen Energy* **2024**, *65*, 817–828. [CrossRef]
100. Perng, T.; Wu, J. A brief review note on mechanisms of hydrogen entry into metals. *Mater. Lett.* **2003**, *57*, 3437–3438. [CrossRef]
101. Tsuru, T.; Huang, Y.; Ali, M.R.; Nishikata, A. Hydrogen entry into steel during atmospheric corrosion process. *Corros. Sci.* **2005**, *47*, 2431–2440. [CrossRef]
102. Kushida, T. Hydrogen Entry into Steel by Atmospheric Corrosion. *ISIJ Int.* **2003**, *43*, 470–474. [CrossRef]
103. Helbert, V.S.; Nazarov, A.; Taryba, M.; Vucko, F.; Montemor, F.; Thierry, D. Kinetics of corrosion reactions on press hardened steel in atmospheric conditions under thin electrolyte films. *Electrochim. Acta* **2023**, *458*, 142500. [CrossRef]
104. Stratmann, M.; Streckel, H.; Kim, K.; Crockett, S. On the atmospheric corrosion of metals which are covered with thin electrolyte layers-iii. the measurement of polarisation curves on metal surfaces which are covered by thin electrolyte layers. *Corros. Sci.* **1990**, *30*, 715–734. [CrossRef]
105. Stratmann, M.; Streckel, H. On the atmospheric corrosion of metals which are covered with thin electrolyte layers—I. Verification of the experimental technique. *Corros. Sci.* **1990**, *30*, 681–696. [CrossRef]
106. Hoar, T. The study of cathodic reactions in metallic corrosion. *ECS Trans.* **1939**, *76*, 157. [CrossRef]
107. Haruna, T.; Shoji, Y.; Hirohata, Y. Hydrogen Absorption Rate into Fe with Rust Layer Containing NaCl during Atmospheric Corrosion in Humidity-controlled Air. *ISIJ Int.* **2021**, *61*, 1079–1084. [CrossRef]
108. Akiyama, E.; Matsukado, K.; Wang, M.; Tsuzaki, K. Evaluation of hydrogen entry into high strength steel under atmospheric corrosion. *Corros. Sci.* **2010**, *52*, 2758–2765. [CrossRef]
109. Akiyama, E.; Li, S.; Shinohara, T.; Zhang, Z.; Tsuzaki, K. Hydrogen entry into Fe and high strength steels under simulated atmospheric corrosion. *Electrochim. Acta* **2011**, *56*, 1799–1805. [CrossRef]
110. Nazarov, A.; Vucko, F.; Thierry, D. Scanning Kelvin Probe for detection of the hydrogen induced by atmospheric corrosion of ultra-high strength steel. *Electrochim. Acta* **2016**, *216*, 130–139. [CrossRef]
111. Ajito, S.; Tada, E.; Ooi, A.; Nishikata, A. Hydrogen absorption behavior of pre-rusted steels under an NaCl droplet. *J. Electrochem. Soc.* **2019**, *166*, C243. [CrossRef]
112. Sørensen, J.; Thorling, L. Stimulation by lepidocrocite (7-FeOOH) of Fe (II)-dependent nitrite reduction. *Geochim. Cosmochim. Acta* **1991**, *55*, 1289–1294. [CrossRef]
113. Schimo-Aichhorn, G.; Traxler, I.; Muhr, A.; Commenda, C.; Rudomilova, D.; Schneeweiss, O.; Luckeneder, G.; Duchaczek, H.; Stellnberger, K.-H.; Faderl, J. Hydrogen insertion into complex-phase high-strength steel during atmospheric corrosion at low relative humidity. *Metals* **2022**, *12*, 624. [CrossRef]
114. Omura, T.; Nakamura, J.; Hirata, H.; Jotoku, K.; Ueyama, M.; Osuki, T.; Terunuma, M. Effect of surface hydrogen concentration on hydrogen embrittlement properties of stainless steels and Ni based alloys. *ISIJ Int.* **2016**, *56*, 405–412. [CrossRef]
115. Ulmer, D.; Altstetter, C. Hydrogen concentration gradients in cathodically charged austenitic stainless steel. *J. Mater. Res.* **1987**, *2*, 305–312. [CrossRef]

116. Alexander Stopher, M.; Rivera-Diaz-del-Castillo, P.E. Hydrogen embrittlement in bearing steels. *Mater. Sci. Technol.* **2016**, *32*, 1184–1193. [CrossRef]
117. Kuhlmann, M.; Schwedler, O.; Holtschke, N.; Jüttner, S. Consideration of hydrogen transport in press-hardened 22MnB5. *Mater. Test.* **2015**, *57*, 977–984. [CrossRef]
118. Kiuchi, K.; McLellan, R. The solubility and diffusivity of hydrogen in well-annealed and deformed iron. In *Perspectives in Hydrogen in Metals*; Elsevier: Amsterdam, The Netherlands, 1986; pp. 29–52.
119. Cheng, X.Y.; Zhang, H.X. A new perspective on hydrogen diffusion and hydrogen embrittlement in low-alloy high strength steel. *Corr. Sci.* **2020**, *174*, 108800. [CrossRef]
120. Dadfarnia, M.; Sofronis, P.; Neeraj, T. Hydrogen interaction with multiple traps: Can it be used to mitigate embrittlement? *Int. J. Hydrogen Energy* **2011**, *36*, 10141–10148. [CrossRef]
121. Silverstein, R.; Eliezer, D.; Glam, B.; Eliezer, S.; Moreno, D. Evaluation of hydrogen trapping mechanisms during performance of different hydrogen fugacity in a lean duplex stainless steel. *J. Alloys Compd.* **2015**, *648*, 601–608. [CrossRef]
122. Tarzimoghadam, Z.; Rohwerder, M.; Merzlikin, S.V.; Bashir, A.; Yedra, L.; Eswara, S.; Ponge, D.; Raabe, D. Multi-scale and spatially resolved hydrogen mapping in a Ni–Nb model alloy reveals the role of the δ phase in hydrogen embrittlement of alloy 718. *Acta Mater.* **2016**, *109*, 69–81. [CrossRef]
123. Dwivedi, S.K.; Vishwakarma, M. Hydrogen embrittlement in different materials: A review. *Int. J. Hydrogen Energy* **2018**, *43*, 21603–21616. [CrossRef]
124. Bhadeshia, H.K.D.H. Prevention of hydrogen embrittlement in steels. *ISIJ Int.* **2016**, *56*, 24–36. [CrossRef]
125. Venezuela, J.; Liu, Q.; Zhang, M.; Zhou, Q.; Atrens, A. A review of hydrogen embrittlement of martensitic advanced high-strength steels. *Corros. Rev.* **2016**, *34*, 153–186. [CrossRef]
126. Jo, K.-R.; Seo, E.-J.; Sulistiyo, D.H.; Kim, J.-K.; Kim, S.-W.; De Cooman, B.C. Data related to dislocation density-based constitutive modeling of the tensile behavior of lath martensitic press hardening steel. *Data Brief* **2017**, *15*, 240–243. [CrossRef] [PubMed]
127. Aucouturier, M. Grain boundary segregations and hydrogen embrittlement. *J. Phys. Colloq.* **1982**, *43*, C6-175–C6-185. [CrossRef]
128. Cho, L.; Seo, E.J.; Sulistiyo, D.H.; Jo, K.R.; Kim, S.W.; Oh, J.K.; Cho, Y.R.; De Cooman, B.C. Influence of vanadium on the hydrogen embrittlement of aluminized ultra-high strength press hardening steel. *Mater. Sci. Eng. A* **2018**, *735*, 448–455. [CrossRef]
129. Li, H.; Lee, C.; Venezuela, J.; Kim, H.-J.; Atrens, A. Hydrogen diffusion and hydrogen embrittlement of a 1500 MPa hot-stamped steel 22MnB5 in different austenitizing conditions. *Mater. Sci. Eng. A* **2024**, *897*, 146349. [CrossRef]
130. Latypova, R.; Nyo, T.T.; Seppälä, O.; Fangnon, E.; Yagodzinskyy, Y.; Mehtonen, S.; Hänninen, H.; Kömi, J.; Pallaspuro, S. Effect of prior austenite grain morphology on hydrogen embrittlement behaviour under plastic straining in as-quenched 500 HBW steels. *Procedia Struct. Integr.* **2022**, *42*, 871–878. [CrossRef]
131. Zhang, S.; Huang, Y.; Sun, B.; Liao, Q.; Lu, H.; Jian, B.; Mohrbacher, H.; Zhang, W.; Guo, A.; Zhang, Y. Effect of Nb on hydrogen-induced delayed fracture in high strength hot stamping steels. *Mater. Sci. Eng. A* **2015**, *626*, 136–143. [CrossRef]
132. Hanninen, H.; Cullen, W.; Kemppainen, M. Effects of MnS inclusion dissolution on environmentally assisted cracking in low-alloy and carbon steels. *Corrosion* **1990**, *46*, 563–573. [CrossRef]
133. Kuniya, J.; Anzai, H.; Masaoka, I. Effect of MnS inclusions on stress corrosion cracking in low-alloy steels. *Corrosion* **1992**, *48*, 419–425. [CrossRef]
134. Kim, M.; Lyu, A.; Jeong, H.-B.; Lee, J.-Y.; Lee, Y.-K. Effect of inclusions on the hydrogen embrittlement of martensitic medium-Mn steel. *J. Mater. Res. Technol.* **2023**, *26*, 2724–2736. [CrossRef]
135. Zhu, X.; Li, W.; Zhao, H.; Wang, L.; Jin, X. Hydrogen trapping sites and hydrogen-induced cracking in high strength quenching & partitioning (Q&P) treated steel. *Int. J. Hydrogen Energy* **2014**, *39*, 13031–13040.
136. Ding, W.; Yang, K.; Gong, Y.; Wang, L.; Hong, J.-y.; Li, W.; Jin, X.-j. Improving hydrogen embrittlement resistance of a modified press hardening steel by introducing retained austenite as hydrogen trap. *J. Iron Steel Res. Int.* **2022**, *29*, 1864–1872. [CrossRef]
137. Malitckii, E.; Yagodzinskyy, Y.; Vilaça, P. Role of retained austenite in hydrogen trapping and hydrogen-assisted fatigue fracture of high-strength steels. *Mater. Sci. Eng. A* **2019**, *760*, 68–75. [CrossRef]
138. Chan, S.; Lee, H.; Yang, J. Effect of retained austenite on the hydrogen content and effective diffusivity of martensitic structure. *Metall. Trans. A* **1991**, *22*, 2579–2586. [CrossRef]
139. Macháčková, N. Corrosion mechanism of press-hardened steel with zinc coating in controlled atmospheric conditions: A laboratory investigation. *Corros. Sci.* **2024**, *240*, 112477. [CrossRef]
140. Hayashida, S.; Mitsunobu, T.; Takebayashi, H. Structure of Surface Oxide Formed on Zinc-Coated Steel Sheet During Hot Stamping. *Corros. Sci. Technol.* **2024**, *23*, 221–227.
141. Volovitch, P.; Allely, C.; Ogle, K. Understanding corrosion via corrosion product characterization: I. Case study of the role of Mg alloying in Zn–Mg coating on steel. *Corros. Sci.* **2009**, *51*, 1251–1262. [CrossRef]
142. Prosek, T.; Thierry, D.; Taxén, C.; Maixner, J. Effect of cations on corrosion of zinc and carbon steel covered with chloride deposits under atmospheric conditions. *Corros. Sci.* **2007**, *49*, 2676–2693. [CrossRef]
143. Talbot, D.E.; Talbot, J.D. *Corrosion Science and Technology*; CRC Press: Boca Raton, FL, USA, 2018.
144. Rudomilova, D.; Prošek, T.; Traxler, I.; Faderl, J.; Luckeneder, G.; Schimo-Aichhorn, G.; Muhr, A. Critical Assessment of the Effect of Atmospheric Corrosion Induced Hydrogen on Mechanical Properties of Advanced High Strength Steel. *Metals* **2020**, *11*, 44. [CrossRef]

145. Liu, Y.; Chen, Y.; Yang, C.; Lian, J.; Feng, Y.; Han, X. The effect of charging conditions on hydrogen embrittlement behavior of ultra-high-strength steel 22MnB5. *Mater. Charact.* **2022**, *194*, 112377. [CrossRef]
146. Chang, Z.; Ruan, X.; Chen, Z.; Zhang, Y.; Li, L.; Lan, L. Comparative evaluation on hydrogen damage behavior of two martensitic high strength press hardening steels. *Int. J. Hydrogen Energy* **2024**, *61*, 1060–1070. [CrossRef]
147. Cao, Z.; Zhang, B.; Huang, M. Comparing hydrogen embrittlement behaviors of two press hardening steels: 2 GPa vs. 1.5 GPa grade. *J. Mater. Sci. Technol.* **2022**, *124*, 109–115. [CrossRef]
148. Wang, M.; Akiyama, E.; Tsuzaki, K. Effect of hydrogen on the fracture behavior of high strength steel during slow strain rate test. *Corros. Sci.* **2007**, *49*, 4081–4097. [CrossRef]
149. Zhang, Z.; Leng, W.; Shao, H.; Zhang, J.; Wang, J.; Cao, C. Study on the behavior of Zn–Fe alloy electroplating. *J. Electroanal. Chem.* **2001**, *516*, 127–130. [CrossRef]
150. Huang, W.; Gu, H.; Liu, Q.; Si, T. Suppression of hydrogen-induced damage in 22MnB5 hot stamping steel by microalloying. *Mater. Chem. Phys.* **2020**, *256*, 123729. [CrossRef]
151. Cho, L.; Kong, Y.; Speer, J.G.; Findley, K.O. Hydrogen embrittlement of medium Mn steels. *Metals* **2021**, *11*, 358. [CrossRef]
152. Krid, M.; Mandy, M.; Sturel, T.; Grigorieva, R.; Drillet, P.; Jacques, P. A better understanding of hydrogen trapping and diffusion in aluminized press-hardenable steels. *J. Mater. Res. Technol.* **2024**, *28*, 1514–1522. [CrossRef]
153. Ootsuka, S.; Tada, E.; Ooi, A.; Nishikata, A. Effect of environmental factors on hydrogen absorption into steel sheet under a wet-dry cyclic corrosion condition. *ISIJ Int.* **2021**, *61*, 1229–1235. [CrossRef]
154. Lee, S.M.; Lee, J.Y. The effect of the interface character of TiC particles on hydrogen trapping in steel. *Acta Metall.* **1987**, *35*, 2695–2700. [CrossRef]
155. Rudomilova, D.; Prošek, T.; Salvetr, P.; Knaislová, A.; Novák, P.; Kodým, R.; Schimo-Aichhorn, G.; Muhr, A.; Duchaczek, H.; Luckeneder, G. The effect of microstructure on hydrogen permeability of high strength steels. *Mater. Corros.* **2020**, *71*, 909–917. [CrossRef]
156. Okayasu, M.; Fujiwara, T. Hydrogen embrittlement characteristics of hot-stamped 22MnB5 steel. *Int. J. Hydrogen Energy* **2021**, *46*, 19657–19669. [CrossRef]
157. Ngiam, Y.; Cao, Z.; Huang, M. Understanding hydrogen embrittlement in press-hardened steel by coupling phase field and hydrogen diffusion modeling. *Mater. Sci. Eng. A* **2022**, *834*, 142523. [CrossRef]
158. Wei, F.-G.; Hara, T.; Tsuzaki, K. Nano-Preciptates Design with Hydrogen Trapping Character in High Strength Steel. In *Advanced Steels: The Recent Scenario in Steel Science and Technology—Proceedings of the International Conference on Advanced Steels (ICAS), Guilin, China, 9–11 November 2010*; Springer: Berlin/Heidelberg, Germany, 2011; pp. 87–92.
159. Gui, L.; Zhao, Y.; Feng, Y.; Ma, M.; Lu, H.; Tan, K.; Chiu, P.-H.; Guo, A.; Bian, J.; Yang, J.-R. Study on the improving effect of Nb-V microalloying on the hydrogen induced delayed fracture property of 22MnB5 press hardened steel. *Mater. Des.* **2023**, *227*, 111763. [CrossRef]
160. Okayasu, M.; Motojima, J. Microstructure-dependent hydrogen diffusion and trapping in high-tensile steel. *Mater. Sci. Eng. A* **2020**, *790*, 139418. [CrossRef]
161. Zhu, X.; Li, W.; Hsu, T.; Zhou, S.; Wang, L.; Jin, X. Improved resistance to hydrogen embrittlement in a high-strength steel by quenching–partitioning–tempering treatment. *Scr. Mater.* **2015**, *97*, 21–24. [CrossRef]
162. Park, J.S.; Bang, H.R.; Jung, S.-P.; Kim, S.J. Effect of plastic strain on corrosion-induced hydrogen infusion and embrittlement behaviors of Zn-coated ultra-high strength steel sheet. *Surf. Coat. Technol.* **2024**, *477*, 130335. [CrossRef]
163. Li, X.; Wang, Y.; Zhang, P.; Li, B.; Song, X.; Chen, J. Effect of pre-strain on hydrogen embrittlement of high strength steels. *Mater. Sci. Eng. A* **2014**, *616*, 116–122. [CrossRef]
164. Nazarov, A.; Vucko, F.; Thierry, D. Scanning Kelvin probe Investigation of high-strength steel surface after impact of hydrogen and tensile strain. *Corros. Mater. Degrad.* **2020**, *1*, 187–197. [CrossRef]
165. Ding, W.; Gong, Y.; Li, W.; Zhu, B.; Zhao, Y.; Jin, X.; Zhang, Y.; Ma, M. Investigation on Mechanical Properties and Hydrogen Behavior Distribution of Nb and V Bearing 22MnB5 B-pillar. In *Advanced High Strength Steel and Press Hardening: Proceedings of the 4th International Conference on Advanced High Strength Steel and Press Hardening (ICHSU2018), Hefei, China, 20–22 August 2018*; World Scientific: Singapore, 2019; pp. 568–578.
166. Yoo, J.; Kim, S.; Jo, M.C.; Kim, S.; Oh, J.; Kim, S.-H.; Lee, S.; Sohn, S.S. Effects of Al-Si coating structures on bendability and resistance to hydrogen embrittlement in 1.5-GPa-grade hot-press-forming steel. *Acta Mater.* **2022**, *225*, 117561. [CrossRef]
167. Kim, S.J.; Park, J.S.; Jung, S.-P. Corrosion-induced hydrogen evolution, absorption, and cracking behaviors of ultra-high-strength galvanized and galvannealed steel sheets. *Mater. Degrad.* **2022**, *6*, 31. [CrossRef]
168. Tada, E.; Miura, Y. Hydrogen Absorption Behavior into Zn and Zn–Al Coated Steels during Corrosion in Aqueous Solutions. *ISIJ Int.* **2016**, *56*, 444–451. [CrossRef]
169. Ma, W.; Li, X.; Zheng, X.; Xu, D.; Zhang, Y.; Yao, Y. Experimental Investigation of Hot Forming of Zn-Coated Hot-Stamping Steel. *Steel Res. Int.* **2004**, *95*, 2400168. [CrossRef]
170. Panagopoulos, C.; Georgiou, E.; Chaliampalias, D. Cathodic hydrogen charging of zinc. *Corros. Sci.* **2014**, *79*, 16–20. [CrossRef]
171. Okayasu, M.; Yang, L. Influence of microstructure on the mechanical properties and hydrogen embrittlement characteristics of 1800 MPa grade hot-stamped 22MnB5 steel. *J. Mater. Sci.* **2019**, *54*, 5061–5073. [CrossRef]
172. Du, Y.; Gao, X.; Lan, L.; Qi, X.; Wu, H.; Du, L.; Misra, R. Hydrogen embrittlement behavior of high strength low carbon medium manganese steel under different heat treatments. *Int. J. Hydrogen Energy* **2019**, *44*, 32292–32306. [CrossRef]

173. Pallaspuro, S.; Fangnon, E.; Aravindh, S.A.; Claeys, L.; Latypova, R.; Yagodzinsky, Y.; Aho, N.; Kantanen, P.; Uusikallio, S.; Depover, T. Mitigating hydrogen embrittlement via film-like retained austenite in 2 GPa direct-quenched and partitioned martensitic steels. *Mater. Sci. Eng. A* **2024**, *908*, 146872. [CrossRef]
174. Persson, D.; Thierry, D.; Karlsson, O. Corrosion and corrosion products of hot dipped galvanized steel during long term atmospheric exposure at different sites world-wide. *Corros. Sci.* **2017**, *126*, 152–165. [CrossRef]
175. Azevedo, M.S.; Allély, C.; Ogle, K.; Volovitch, P. Corrosion mechanisms of Zn (Mg, Al) coated steel in accelerated tests and natural exposure: 1. The role of electrolyte composition in the nature of corrosion products and relative corrosion rate. *Corros. Sci.* **2015**, *90*, 472–481. [CrossRef]
176. Azevedo, M.S.; Allély, C.; Ogle, K.; Volovitch, P. Corrosion mechanisms of Zn (Mg, Al) coated steel: 2. The effect of Mg and Al alloying on the formation and properties of corrosion products in different electrolytes. *Corros. Sci.* **2015**, *90*, 482–490. [CrossRef]